Behavior of oil droplets at the membrane surface during crossflow microfiltration of oil-water emulsions

Accepted for publication[1] in the Journal of Membrane Science on Nov 7, 2015.
Published article DOI: 10.1016/j.memsci.2015.11.005

Emily N. Tummons[a], Volodymyr V. Tarabara[a*], Jia Wei Chew[b,c], Anthony G. Fane[c,d]

[a] Department of Civil and Environmental Engineering, Michigan State University, East Lansing, MI 48824, USA
[b] School of Chemical and Biomedical Engineering, Nanyang Technological University, Singapore, 637459
[c] Singapore Membrane Technology Centre, Nanyang Environment and Water Research Institute, Nanyang Technological University, Singapore, 637141
[d] School of Civil and Environmental Engineering, Nanyang Technological University, Singapore, 639798

Email addresses:
tummonse@msu.edu (ENT)
tarabara@msu.edu (VT)
jchew@ntu.edu.sg (JWC)
a.fane@unsw.edu.au (AGF)

*Corresponding author: Phone: +1 (517) 432-1755

---

[1] Full citation: Tummons, E. N.; Tarabara, V. V.; Chew, J.-W.; Fane, A. G. Behavior of oil droplets at the membrane surface during crossflow microfiltration of oil-water emulsions. J. Membr. Sci. 500 (2016) 211-224.

Abstract

A fundamental study of microfiltration membrane fouling by emulsified oil was conducted using a combination of real-time visualization, force balance on a droplet, and permeate flux analysis. The model 0.1% v/v hexadecane-in-water emulsions contained sodium dodecyl sulfate (0.1 mM, 0.4 mM, or 0.8 mM) to regulate interfacial tension. Direct Observation Through the Membrane tests with Anopore (d_{pore} = 0.2 μm) and track-etch (d_{pore} = 5 μm) membranes revealed three characteristic stages of membrane fouling: 1) droplet attachment and clustering, 2) droplet deformation, and 3) droplet coalescence. In qualitative agreement with visualization results, the force balance predicted that droplets $\lesssim$ 36 to 40 μm would remain pinned at d_{pore} = 5 μm pores while larger droplets would be swept off the surface by the crossflow drag. In a separate set of constant pressure crossflow filtration tests with track-etch membranes, the average oil rejection was ≥ 98% while the permeate flux decreased to a pseudo-steady-state ~10% of the initial value. The results indicate that membrane fouling by emulsified oil is controlled by droplet coalescence and crossflow shear: the transport of oil to the membrane surface by the permeate flow is balanced by the shear-induced removal of the droplets that coalesce to exceed a critical size.

Keywords: oil-water separation; microfiltration; crossflow filtration; direct observation through membrane (DOTM); force balance.

1. Introduction

Porous membranes were first used for the treatment of oily wastewaters in the early 1970s [1-3]. Since then, research on the separation of oil-water emulsions by microfiltration (MF) and ultrafiltration (UF) membranes has been growing (Figure 1; also see Supplementary material, Figure S1); thus enabling industrial applications [4-6]. A broad variety of MF [4, 7-12] and UF [3, 8, 13-19] membranes have been evaluated. Membrane materials ranged from polymers [7, 9, 14, 15] to ceramics [8, 13, 18, 19] to metals [10], while membrane configurations and types included flat sheet [14, 15], tubular [3, 8-10, 16, 18, 19], hollow fiber [7], track-etch [11], and slotted pore filters [12] as well as microchannel cells [20, 21]. Synthetic emulsions containing various types of oil (e. g., cutting oil [7, 9], crude oil [12, 13, 17, 19], diesel oil [19], dodecane [22], mineral oil [15], kerosene [11, 23], and edible oils [12, 16, 18]), liquid-liquid food emulsions (e. g., skimmed milk [24]) and industrial oily wastewaters (e. g., bilge water [1], metal rolling mill wastewater [25], and produced water [6, 26, 27]) were employed.

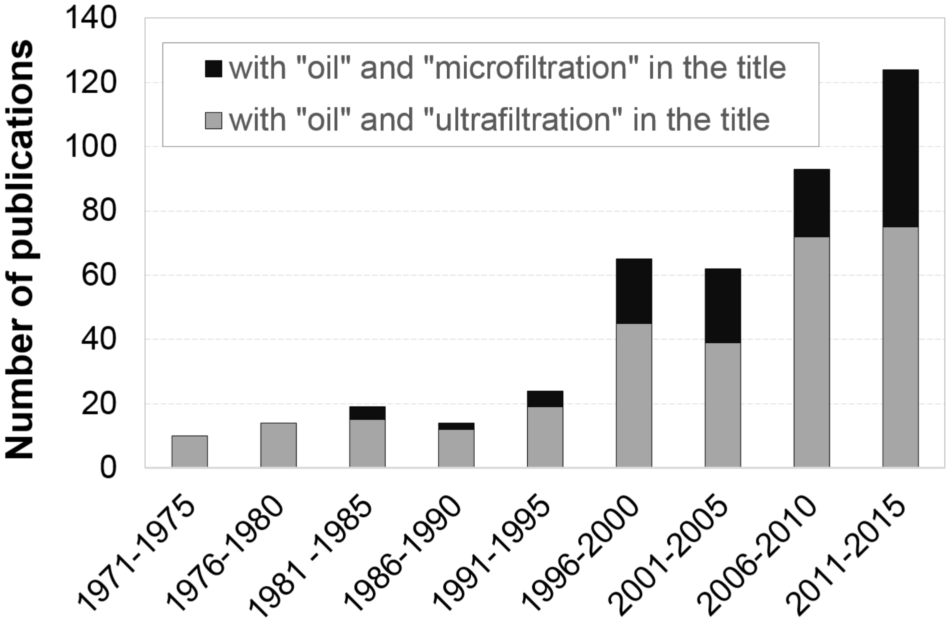

Figure 1: Number of publications with a) both “oil” and “ultrafiltration” in the title and b) both “oil” and “microfiltration” in the title. Source: Google Scholar. Retrieved: November 1, 2015.

An industrial wastewater of emerging concern is produced water, a byproduct of oil and gas extraction processes; in 2007, the global produced water output was estimated to be ~250 million barrels per day [28]. Produced water has a very complex composition including suspended oil (typically, 100 to 5,000 mg/L), high salinity and various chemicals added for operational purposes. Because a substantial fraction of oil in produced water can be in the emulsified form [29], membrane separation is one of the few technologies capable of removing the small oil droplets [30, 31] to meet the discharge limit (15 to 40 mg(oil)/L depending on the country and location of the platform [32]). While membranes with sufficiently small pores can separate such emulsified oil from water the issue of membrane fouling has prevented a broader acceptance of membranes. In the case of liquid-liquid emulsions, the issues of droplet stability, shape, and compressibility make the already complex fouling phenomena more challenging to understand and manage.

A number of mechanistic dead-end filtration studies showed that oil droplets rejected by a membrane form a concentrated oil-water emulsion at the membrane surface [14, 15, 21, 23, 33, 34]. The deposit has been described as a gel layer but also referred to as a “cake”. Lipp et al. concluded that for oil feed concentrations <10% (v/v) the permeate flux follows gel-polarized behavior that can be described by a film model [15]. Matsumoto et al. showed that the gel layer was highly compressible and had specific hydraulic resistances that were 2 to 3 orders of magnitude higher than that of yeast and polymethyl methacrylate particles [21]. Working with non-coalescing kerosene-water emulsions, Iritani et al. observed the formation of a highly compressible gel layer that may have porosity much lower (~0.02) than that of a hexagonal close packing of non-deformed spheres (0.2595) [23]. The fouling layer structure was quantified based on indirect evidence such as measured values of oil rejection and rate of permeation through fouled membranes; the specific hydraulic resistance of the fouling layer was calculated based on equations initially derived for solid-liquid separations [35, 36], which may explain the use of the term “cake” by several groups. Blocking filtration laws were also applied to analyze mechanisms of membrane fouling in several studies [19, 37-39], but with regard to the intrapore fouling this approach is questionable because the laws were derived for spherical and non-deformable particles. Direct visualization of oil droplets in a microchannel filtration cell [20, 21] confirmed that deformability has a strong impact on the separation performance: droplets larger than membrane pores were shown to permeate the membrane at sufficiently high pressures. In the visualization work with micro channels, the size of oil droplets was either much smaller (1.5 μm for primary droplets) or much larger than the pore size (3.8 μm) and no buildup of a multilayer of rejected droplets was observed; thus it was neither possible to explore the effect of the variable headloss across the fouling layer nor was it possible to verify other potential permeation scenarios (e. g., percolation through a contiguous oil film).

In tangential filtration the structure of the fouling layer depends on additional transport mechanisms enabled by the crossflow. Crossflow filtration behavior of oil-water emulsions was shown to be similar to that of macromolecular solutions [16]. As demonstrated in multiple studies [13, 16, 22, 40-42] the permeate flux achieves a steady state value indicating that there is balance between convective transport of oil droplets to the membrane surface with the permeate flow and oil back-transport away from the membrane [13, 39]. NMR chemical shift selective micro-imaging was successfully applied to non-invasively visualize fouling layer in crossflow microfiltration [7, 9, 43]; it was demonstrated that a concentration polarization layer is present and slowly flows along the membrane surface [43]. The spatial resolution of the method (39 μm [7], 94 μm [43]), however, was not sufficient to discern droplet-scale features of the fouling layer.

Recent modeling studies explored the effect of crossflow on the behavior of an individual oil droplet pinned at a membrane micropore [44, 45]. Three main scenarios (permeation, rejection, and breakup/partial permeation) for oil droplets were identified and shown to depend on the droplet size, shear rate, surface tension, and oil-to-water viscosity ratio. To our knowledge there have been no visualization studies that assessed such scenarios experimentally. Useful insights can be gained from the experimental and computational modeling work on membrane emulsification (e.g. [46, 47]) where a related problem is considered wherein microfilters are used to form controllable oil droplets as oil is extruded through the membrane.

The present study is motivated by the need for a better droplet-scale understanding of membrane fouling by emulsified oil. To this end, we employ a combination of real-time visualization, force balance on a droplet, and permeate flux analysis. Direct Observation Through the Membrane (DOTM) [48, 49] is used to image oil droplets at the membrane surface and visualize, in real time, the fouling layer as it forms and develops throughout the crossflow filtration process. To gain a quantitative insight into oil droplet behavior at the membrane surface, we use a simple force balance analysis and carry out a separate set of well controlled constant pressure crossflow filtration tests to understand the kinetics of permeate flux decline under the condition of membrane fouling by oil.

Materials and Methods

2.1 Reagents

Hexadecane (99%) and sodium dodecyl sulfate (SDS, ≥98.5%) were purchased from Sigma-Aldrich and used as received. Deionized (DI) water used in all DOTM experiments was supplied by a Milli-Q Ultrapure Water (Integral 10, Millipore) system equipped with a terminal 0.2 μm microfilter (MilliPak, Millipore); the water resistivity was approximately 18 MΩ·cm. Prior to the constant pressure crossflow tests, the DI water was filtered through a 0.2 μm microfilter (PolyCap, Whatman). Hydrochloric acid (HCl, EMD Chemicals) was diluted to 2 M before being used in the oil extraction process. Tetrachloroethylene (ultra resi-analyzed) was purchased from J.T. Baker and used as received.

2.2 Preparation and characterization of oil-in-water emulsions

The model emulsions were prepared by adding hexadecane to water in the presence of SDS as a stabilizing agent and stirring the resulting mixture at 1,000 rpm using a digital stand mixer (RW 20 digital dual-range mixer, IKA) for 20 minutes. Hereinafter the hexadecane-water-surfactant emulsions will be referred to as HWS-X where X is the concentration of SDS in units of mM. In all emulsions the hexadecane concentration was 0.1% v/v (773 mg/L), while the concentration of SDS was either 0.1 mM (HWS-0.1 emulsion) or 0.4 mM (HWS-0.4 emulsion) or 0.8 mM (HWS-0.8 emulsion). The hexadecane was dyed red with Oil-Red-O dye (Sigma-Aldrich) prior to the constant pressure crossflow tests to aid in oil rejection measurements. Light scattering (Malvern Mastersizer 2000) was used to determine oil droplet size distribution in the feed emulsion using undyed hexadecane. The feed was continuously circulated through the optical cell of the Mastersizer using a Malvern sample dispersion unit mixed at 1,000 rpm. The refractive index of 1.434 for hexadecane was used as an input in the calculation of droplet size distribution. The volume-based distribution reported by the Mastersizer software was converted into a number-based distribution.

The interfacial tensions of the three emulsions were measured using a pendant drop method and a standard goniometer (model 250-F4, ramé-hart instrument co.). First, the surface tensions of the pure liquids (water and hexadecane) and the aqueous solutions of SDS were determined; as the results would later be used by the DROPimage Advanced v2.6 software during the interfacial tension measurements. A microsyringe (part no. 100-10-20) was filled with each of the liquids, which was then dispensed until a hanging pendant droplet was produced; the surface tension of the liquid was determined based on the droplet's shape as quantified by the software. The interfacial tension measurements were performed by filling the standard quartz cell (part no. 100-07-50) with each of the aqueous solutions of SDS and using a microsyringe with inverted stainless steel 22g needle (part no. 100-10-13-22) filled with hexadecane to produce a submerged pendant droplet. The interfacial tensions of the emulsions were determined by the software based on the shape of the submerged hexadecane droplets in the aqueous solutions of SDS.

2.3 Membranes used in DOTM and constant pressure crossflow filtration tests

Two types of hydrophilic microfilters were used: inorganic anodized alumina (Anopore) membranes with a nominal pore diameter of 0.2 μm and polycarbonate track-etch (PCTE) membranes with a nominal pore diameter of 5 μm. When wet, membranes of both types had sufficient optical transparency required in the DOTM method. The anodic alumina Anopore microfilter (Anodisc membrane filters, Whatman) has surface porosity (as reported by the manufacturer) in the 25 to 50% range and a non-deformable honeycomb pore structure with no lateral crossovers between individual straight-through pores. The other membrane chosen for the DOTM tests was the PCTE membrane (Nuclepore, Whatman) with cylindrical and narrowly distributed straight-through pores and a surface porosity of 7.9%. The PCTE membranes were treated with polyvinylpyrrolidone (PVP) by the manufacturer to create the hydrophilic surface. Table 1 summarizes manufacturer-supplied data for the membranes as well as several other characteristics that can be calculated based on simple geometrical considerations.

Table 1: Morphological characteristics of the polycarbonate track-etch (PCTE) and Anopore membranes employed in this study
provided by the manufacturer
† applies to all PCTE membranes used in this study regardless of the supplier

Membrane characteristic	**Membrane**	
	PCTE†	**Anopore**
Pore diameter#, μm	5	0.2
Surface pore density#, pores/cm^2	$4 \cdot 10^5$	$1 \cdot 10^9$
Area of one pore, cm^2	$1.96 \cdot 10^{-7}$	$3.14 \cdot 10^{-10}$
Surface porosity, %	8	31
Average membrane area per one pore, cm^2	$2.50 \cdot 10^{-6}$	$1.00 \cdot 10^{-9}$
Average distance between pore centers, μm	15.8	0.32
Average distance between pore boundaries, μm	10.8	0.12

The crossflow filtration tests required a larger membrane area than the 47 mm diameter Anopore or Nuclepore membrane discs could provide, so only an alternative manufacturer's PCTE membranes (Sterlitech) with the same morphological characteristics were used in these experiments. A new membrane was used in each test.

The contact angles of hexadecane on the two membranes were measured using a standard goniometer (model 250-F4) and specialized tools provided by the ramé-hart instrument co. Each membrane was attached to the environmental fixture (part no. 100-14) with the feed side facing downward and then submerged in water when the fixture was placed in the standard quartz cell (part no. 100-07-50). The microsyringe (part no. 100-10-20) was filled with hexadecane and a single droplet was dispensed from the inverted stainless steel 22g needle (part no. 100-10-13-22 until the droplet attached to the submerged inverted membrane. This process used the DROPimage Advanced v2.6 software to measure the contact angle between the hexadecane droplet and the membrane surface in the presence of water.

2.4 Direct Observation Through the Membrane system

Figure 2A shows the schematic of the DOTM setup. The central feature of the DOTM system is the microscope (Axio Imager.M1, Zeiss) fitted with a video camera (Digital Color video camera model TK-C921BEG, JVC) capable of capturing both still images and videos. All of the images and videos recorded during filtration tests used a 32X magnification microscope objective resulting in a total magnification of 320X. A crossflow membrane filtration cell included two acrylic windows to enable imaging of the membrane surface. The crossflow channel in the DOTM filtration cell was 109 mm long, 33.5 mm wide and 2 mm deep. Both Anopore and PCTE disk membranes with diameters of 47 mm were framed between two pieces of paper with a square cutout for the membrane in the center of the crossflow channel to facilitate the use of circular membrane disks in the rectangular crossflow channel. Araldite 2020 adhesive (Huntsman) was used to secure the membrane between the papers so that an active membrane area of 7.56 cm^2 was available for tests with Anopore, while a slightly smaller active membrane area of 2.4 cm^2 was used for tests with PCTE membranes due to the difficulty of imaging the flexible membrane. The framed membrane was held between the two acrylic sides of the filtration cell and secured to the stage of the microscope with the permeate side of the membrane facing up towards the objective. The light emitted by the microscope's illuminator transmitted through the membrane as the images were captured by focusing through the membrane and onto its feed side. The crossflow and permeate fluxes were adjusted independently using a feed gear pump (drive model 75211-15, Cole-Parmer) and a permeate peristaltic pump (Minipuls 3, Gilson). Three pressure sensors (Cole-Parmer) were interfaced with a computer to monitor the pressure immediately upstream of the membrane in the feed line and downstream of the membrane in both the retentate and permeate lines. The permeate was collected on an electronic mass balance (PL4002, Mettler Toledo) interfaced with a computer that recorded values of permeate mass at 1 min intervals. DOTM experiments were carried out at a constant crossflow velocity of $3.6 \cdot 10^5$ L/($m^2 \cdot h$) (0.1 m/s) that translated to the Reynolds number, Re = 376. Higher crossflow velocities could not be tested because Anopore membranes were too brittle to withstand an immediate increase to high crossflow velocities; when the crossflow velocity was increased slowly the membrane became fouled before the target higher crossflow velocity (0.7 m/s) could be reached.

Throughout each DOTM experiment, the permeate rate was incrementally increased by adjusting the permeate pump setting to screen a range of fouling conditions. The continual increase in the permeate flux and the buildup of hydraulic resistance due to membrane fouling by oil led to an increase in the headloss across the membrane. Thus, the DOTM experiments could not be classified as constant pressure or constant flux filtration tests.

2.5. Crossflow microfiltration system

Constant pressure crossflow microfiltration experiments were performed using a separate crossflow filtration system (Figure 2B). The filtration cell (CF042, Sterlitech) had a membrane area of 40.95 cm^2 and a crossflow channel that was 105 mm long, 39 mm wide and 2.3 mm deep. A gear pump (drive model 75211-10, Cole Parmer) delivered the feed emulsion to the membrane filtration cell at a constant crossflow velocity of $3.6 \cdot 10^5$ L/($m^2 \cdot h$) (0.1 m/s) matching the crossflow velocity used in DOTM tests. The corresponding Reynolds number was higher (Re = 433) than in DOTM experiments (Re = 376) because of differences in the crossflow channel dimensions. The retentate flow was directed back into the feed tank.

Permeate samples were collected and oil contents in the samples were measured to determine oil rejection by the membrane. For each experiment, six permeate samples were taken, one every 15 minutes throughout the first 1.5 h of the 2 h test, along with one sample of the initial feed emulsion. The permeate was directed to a beaker positioned on a mass balance (Adventurer Pro AV812, OHAUS Corp. USA) and the data were automatically logged into a computer. All experiments were performed in triplicate.

2.6 Measurements of oil rejection by the membrane

The oil contents in both the feed emulsion and the permeate were measured for each crossflow test using a solvent extraction method. The solvent extraction procedure involved mixing the oil-in-water sample with tetrachloroethylene to extract oil into the organic phase; the method required an initial sample volume of at least 24 mL to ensure that the cuvettes could be filled properly for the measurements because only the organic solvent portion of the sample was analyzed. The initial samples could be diluted with DI water to achieve the minimum sample volume as long as the oil concentration remains above the detection limit. The feed samples (4 mL) taken before each crossflow test were diluted to one tenth of the initial concentration using DI water to achieve an excess of the necessary sample volume. In each of the crossflow tests, the six permeate samples (~4 mL) taken throughout the filtration were combined so that the oil content in the permeate could be measured without diluting the samples. The pH of each sample was adjusted to less than 2 by adding 2 M HCl dropwise, and then tetrachloroethylene was added in the 1:10 v/v proportion with respect to the sample. Next, the samples were shaken for 2 min. Once the solvent containing the dyed oil separated to the bottom of the vials it was extracted using a syringe and dispensed into a cuvette for analysis.

The oil content was determined using two separate detection methods: infrared spectroscopy (InfraCal oil in water analyzer, model CVH, Wilks) and UV-Vis spectrophotometry (MultiSpec-1501, Shimadzu). The dual detector in the InfraCal analyzer measures hydrocarbon concentrations at 2940 cm^{-1} with a reference at 4,000 cm^{-1}. In the UV-Vis method, oil concentration was measured based on absorption at 518 nm (maximum absorption of Oil-Red-O dye). The oil detection limits of the InfraCal and UV-Vis methods were 2 mg/L and 4.5 mg/L, respectively. The observed rejection of oil by the membrane was calculated as $R = 1 - \frac{C_p}{C_f}$ where C_p the concentration of oil in the permeate and C_f is the initial concentration of oil in the feed emulsion.

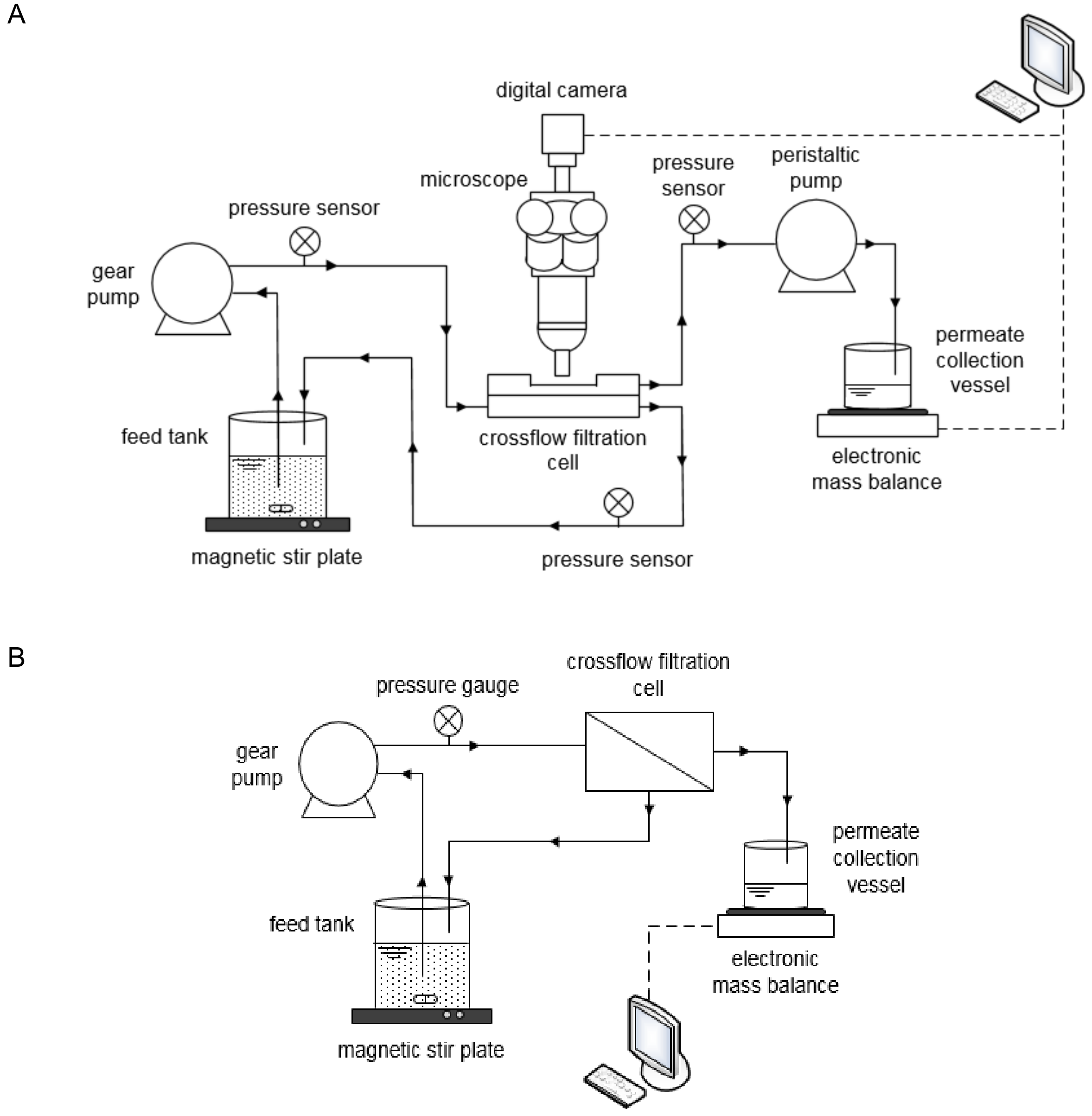

Figure 2: Schematic illustration of the Direct Observation Through the Membrane (DOTM) apparatus (A) and the crossflow microfiltration system (B).

3. Results and Discussion

3.1 Characteristics of oil emulsions and membranes. Critical pressure for oil droplet entry into a pore

The tabulated values of the surface tensions for DI water and hexadecane are 72.8 mN/m and 27.6 mN/m [50]. The interfacial tension of hexadecane and water was measured to be 41.8 mN/m. The surface tension of the three aqueous solutions of SDS were measured to be 69.4, 66.5, and 56.9 mN/m for SDS concentrations of 0.1 mM, 0.4 mM, and 0.8 mM, respectively. These values were below the critical micelle concentration for SDS, which is in the 6 mM to 8 mM range. Based on these measurements, the interfacial tensions of the HWS-0.1, HWS-0.4 and HWS-0.8 emulsions were determined to be 39.3 mN/m, 35.0 mN/m, and 30.8 mN/m, respectively. It was assumed in this work that coalescence-induced desorption of surfactant was sufficiently fast to make the resulting transient changes in the interfacial tension relatively unimportant. The droplet size distributions (Figure 3) illustrate the effect of droplet stability on emulsion characteristics. The volume weighted mean values for the HWS-0.1, HWS-0.4 and HWS-0.8 emulsions were 109 μm, 105 μm and 93 μm. The volume-based median droplet diameter also decreased with the increase in droplet stability from 104 μm to 90 μm to 71 μm for the HWS-0.1, HWS-0.4 and HWS-0.8 emulsions, respectively. Comparison of size distribution measurements obtained in duplicate tests showed that the variation in the values of the volume-weighted mean was 1.6%, 6.8% and 17.7% for the HWS-0.1, HWS-0.4 and HWS-0.8 emulsions, respectively.

The contact angle of hexadecane on the Anopore membrane surface was 152° and 154° in 0.1 mM SDS and 0.8 mM SDS solutions, respectively, and 151° in the absence of SDS. For the PCTE membrane, the hexadecane contact angle was measured to be 135° and 147° in 0.1 mM SDS and 0.8 mM SDS solutions, respectively, while in the absence of SDS the contact angle was 120°. Thus, both membranes were oleophobic, while the Anopore membrane could be qualified as superoleophobic [51].

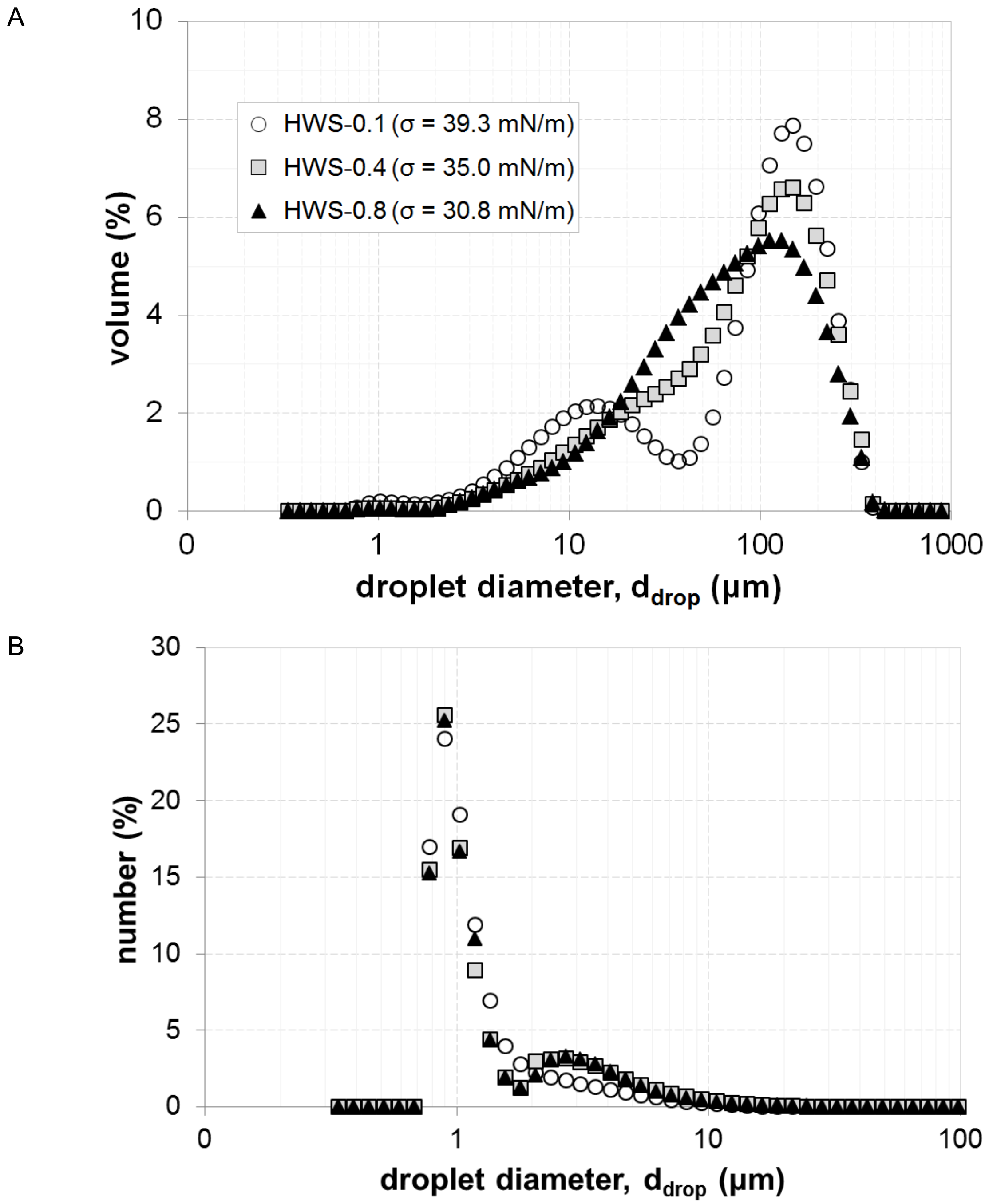

Figure 3: Volume-based (A) and number-based (B) droplet size distributions for the three SDS-stabilized hexadecane-water emulsions used in the DOTM and constant pressure microfiltration tests.

The critical pressure required for an oil droplet of diameter, d_{drop}, to enter a circular pore of diameter, d_{pore}, is given by [8]

$$\Delta P_{\text{crit}} = 4\sigma \frac{\cos\theta}{d_{\text{pore}}}\left[1 - \left(\frac{2 + 3\cos\theta - \cos^3\theta}{4\left(\frac{d_{\text{drop}}}{d_{\text{pore}}}\right)^3 \cos^3\theta - (2 - 3\sin\theta + \sin^3\theta)}\right)^{1/3}\right] \tag{1}$$

In eq. (1), σ is the interfacial tension and $\theta = 180° - \varphi$ where φ is the contact angle between the surface of the membrane and the oil droplet at the oil/water interface. Eq. (1) is valid for a single non-wetting droplet pinned at an entry to a single membrane pore

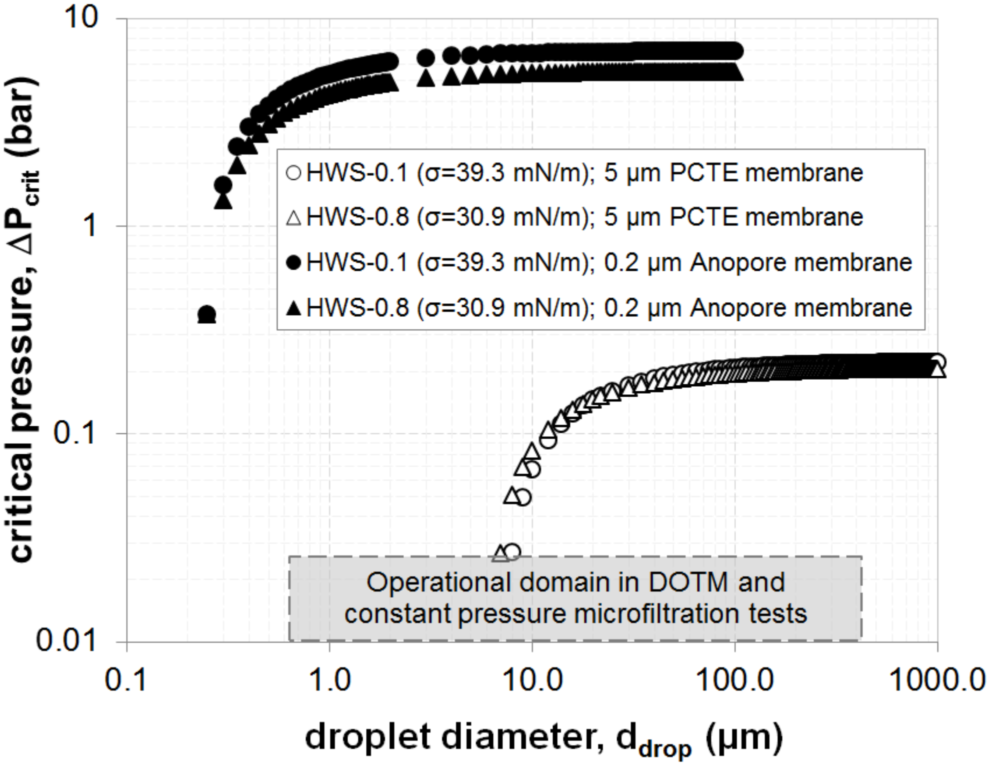

Figure 4: Critical pressure for an oil droplet to enter a membrane pore as a function of oil droplet size, membrane pore size, and interfacial tension of the oil-water emulsion. The calculation is based on eq. (1) and is for Anopore (d_{pore} = 0.2 µm) and polycarbonate PCTE (d_{pore} = 5 µm) membranes. The operational domain represents the range of oil droplet sizes in the HWS-0.1 and HWS-0.8 emulsions and the range of transmembrane pressures employed in the DOTM and constant pressure microfiltration tests.

In a computational modeling study, Darvishzadeh and Priezjev [44] have shown that numerical simulations of droplet permeation in the absence of crossflow predict ΔP_{crit} value that matches well to the value given by eq. (1).

Figure 4 shows how the critical pressure, ΔP_{crit}, given by eq. (1) depends on the droplet diameter. The grayed out area corresponds to the values of transmembrane pressures (ΔP) and droplet sizes (d_{drop}) in the DOTM and constant pressure microfiltration tests. For the Anopore membranes (d_{pore} = 0.2 μm), $\Delta P/\Delta P_{crit}$ ~10^{-2}; therefore, complete rejection of oil by these membranes could be expected and was indeed experimentally observed (see section 3.3.2). It is important to note, however, that eq. (1) was derived assuming zero crossflow on the feed side of the membrane [8, 11]. Darvishzadeh and Priezjev [44] predicted that ΔP_{crit} should increase with an increase in crossflow velocity up to a certain threshold value when the droplet breaks up. We also note that Figure 3 provides an estimate of the actual droplet size distribution, which is dynamically changing in the membrane channel due to droplet break-up and coalescence.

In experiments with PCTE membranes (d_{pore} = 5 μm), ΔP exceeded ΔP_{crit} for smaller droplets ($d_{drop} \lesssim$ 10 μm). Based on the fraction of oil mass that is in these smaller droplets (Figure 3A), the oil rejection by PCTE membranes was estimated to be ~86.3%, 92.1%, and 92.8% for HWS-0.1, HWS-0.4, and HWS-0.8 dispersions, respectively. Experimentally measured rejections were somewhat higher (see section 3.3.1), which can be attributed to the effects of crossflow and droplet coalescence that are not accounted for by eq. (1). It is also possible that the ensemble of droplets that reached the membrane was not representative of the entire droplet population as measured by light scattering or that a fraction of the entire oil mass in the feed was not transported to the membrane. The tendency for larger particles to migrate from the membrane and smaller ones to deposit was observed for latex particles via DOTM by Li et al. [48].

3.2 Characteristic stages of membrane fouling by emulsified oil. Capillary number

Representative DOTM images capturing the interaction of the oil droplets with the polycarbonate track-etch membrane (d_{pore} = 5 μm) are shown in Figure 5. Each of the three rows of images corresponds to a filtration experiment with an emulsion with a different concentration of surfactant (0.1, 0.4, or 0.8 mM) and, accordingly, different interfacial tension (39.3, 35.0, or 30.9 mN/m). The first column (Figure 5 A, E, I) shows images of clean membranes. Elongated ovals or cylinders correspond to pores that are at an angle to the membrane surface. A magnified view of the PCTE membrane pores is shown in the inset A.1 of Figure 5. The three images in the first column (Figure 5 A, E, I) correspond to *t* = 0. All other images (columns 2, 3 and 4) represent different fouling stages that occur at different times into an experiment depending on the concentration of the surfactant (see Figure 8 for time stamps).

DOTM experiments with hexadecane-water-SDS emulsions revealed three characteristic stages of membrane fouling: 1) droplet attachment and clustering, 2) droplet deformation, and 3) droplet coalescence:

1) *Droplet attachment and clustering* (Figure 5 B, F, J) occurs during the early stages of membrane fouling by emulsified oil. A typical clustering scenario involves accumulation of smaller droplets around a previously attached larger droplet that is most often pinned at a pore entry.
2) As a droplet cluster grows, the constituent droplets press against one another and deform, attaining increasingly angular, polyhedral shapes. These transient phenomena can be described as the *droplet deformation* stage (Figure 5 C, G, K).
3) Continued deformation of neighboring droplets leads to thinning of the water film in between them until the film ruptures and droplets merge [52]. This *droplet coalescence* stage (Figure 5 D, H, L) continues with larger droplets growing at the expense of smaller ones. In tests with PCTE

membranes (d_{pore} = 5 μm), some of the coalesced droplets grew to be as large as ~95 μm covering multiple pores (Figure 5D).

We note that the three stages overlap in time (see section 3.4).

3.2.1. Capillary and Bond numbers. Droplet deformation and breakup

The propensity of a droplet to deform due to crossflow can be estimated using the capillary number, Ca, defined as a ratio of the viscous and interfacial tension forces:

$$Ca_{cf} = \frac{\mu_w d_{drop} \dot{\gamma}}{\sigma} \tag{2}$$

where μ_w is the viscosity of the dispersion phase (water) and $\dot{\gamma}$ is the shear rate at a distance $y = \frac{1}{2} d_{drop}$ away from the membrane surface. Because the width of the membrane channel is much larger than its height ($W \gg H$) we approximate the flow field by plane Poiseuille flow between two infinite parallel stationary plates separated by distance H. This approximation gives the following expression for the shear rate (see Supplementary material):

$$\dot{\gamma} = \left[\frac{dv_x}{dy}\right]_{y=\frac{1}{2}d_{drop}} = \frac{1}{2\mu_w}\frac{dP}{dx}\left(H - d_{drop}\right) = 6\frac{\bar{v}_x}{H}\left(1 - \frac{d_{drop}}{H}\right) \tag{3}$$

For the experimental conditions of DOTM tests, Ca_{cf} ranged from $4.9 \cdot 10^{-6}$ to $4.6 \cdot 10^{-4}$ for the range of droplet sizes observed on the membrane surface (1 μm to 95 μm). Another viscous force that acts on a droplet at a membrane surface is the drag due to the permeate flux. The importance of this effect relative to surface tension forces can be estimated using the capillary number defined as follows:

$$Ca_{pf} = \frac{\mu_w j}{\sigma} \tag{4}$$

where j is the permeate flux. For permeate fluxes employed in DOTM experiments ($1 \cdot 10^{-6}$ m/s $\leq j \leq 9 \cdot 10^{-5}$ m/s), Ca_{pf} ranged from $\sim 3.3 \cdot 10^{-8}$ to $\sim 2.9 \cdot 10^{-6}$. The effect of the gravitational and buoyancy forces on the droplet shape can be estimated using the Bond number, $Bo = (\rho_w - \rho_{oil}) r_{drop}^2 g / \sigma$. For the largest droplets observed in DOTM tests (d_{drop} = 95 μm) and the highest concentration of surfactant (0.8 mM; σ = 30.5 mN/m), $Bo \cong 7 \cdot 10^{-4}$. These calculations are based on the approximation of droplets as spherical objects. The droplets are, generally, non-spherical. The contact angle of the membrane will have an effect on the droplet's shape, although both the Anopore and PCTE membranes are oleophobic causing the pinned droplets to keep a mostly spherical shape. Peng and Williams' work on membrane emulsification explains how droplets can become slightly distorted due to the presence of the pore and local hydrodynamic forces arising from the crossflow [46]; these authors also note that the buoyancy force might slightly change the shape of the droplet depending on the relative magnitude of all of the forces (see section 3.6).

DOTM tests offered direct experimental evidence of droplet deformation. Thus, even though viscous and body forces were relatively small (Ca_{cf}, Ca_{pf}, Bo <<1) and incapable of breaking droplets up, these forces were sufficient to change droplet shape. This effect can be partly due to the compressive forces (in the direction along the membrane surface) that are accumulative - the stress due to the drag force is transmitted through the points or areas of contact between droplets along the sequence of adjacent droplets and in the direction of the crossflow so that the highest stress is experienced by the droplet pinned at the pore entry. Such accumulating solid compressing force is a reason for compression and restructuring of membrane cakes (e. g, [53, 54]) with the difference that the drag force on particles in the membrane cake acts in the direction normal to the membrane surface. Brans et al. used CFD modeling to show that the drag force exerted by the crossflow on a particle (or, in our case, a droplet) decreases as the membrane surface coverage increases, implying that there is a shielding effect [55]. The shielding effect results in increased blockage of the pores located further downstream in the direction of the crossflow due to the decreased drag force experienced by the attaching droplets. The shielding effect might also help to explain the clustering of droplets on the membrane surface during early stages of membrane fouling.

Droplet deformation was observed for both PCTE and Anopore membranes and did not appear to depend on the membrane type despite differences in the permeate flow patterns near attached droplets. We attribute this to the fact that the permeate flux was relatively small in relation to the crossflow flux (so that $Ca_{pf} \ll Ca_{cf}$) as is typical for most crossflow filtration systems. In dead-end filtration the membrane type may make a difference though. The average distance between pores of the PCTE membrane is ~2 orders of magnitude larger than the corresponding value for the Anopore membranes (10.8 μm versus 0.1 μm; Table 1) indicating that the stagnation point flow due to permeation enhances $\dot{\gamma}$ more in the case of PCTE membranes. This difference should be even more pronounced due to the fact that surface porosity of the Anopore membrane was 3.875 times higher than that of the PCTE membrane: the lower surface porosity of the PCTE membrane translates into higher "pore velocity" and higher local velocity close to the pore entrance.

3.3 Effect of interfacial tension on oil droplet behavior at the membrane surface

3.3.1 Microfiltration with polycarbonate track-etch membranes (d_{pore} = 5 μm)

Figure 5 demonstrates the impact that surfactant had on oil droplet coalescence and membrane fouling for a PCTE membrane. Increasing the concentration of surfactant lowers the interfacial tension causing the droplets to breakup more easily during the formation of the emulsion (see Figure 3), while at the same time limiting the coalescence of newly formed droplets. Both of these effects translate into distinctly different behaviors of the droplets at the membrane surface (Figure 5). Images in the first row (Figure 5 B, C, D) depict the membrane surface during filtration of an HWS-0.1 emulsion, composed of droplets that are on average larger than droplets in HWS-0.4 and HWS-0.8 emulsions and that tend to eventually coalesce into very large droplets covering multiple pores. As observed in the field of view of the DOTM microscope, HWS-0.1 droplets deposited on the membrane surface ranged from 2 μm to 20 μm in size initially and over the ~1.5 h of filtration coalesced into droplets as large as 95 μm. (A video of the oil droplets coalescing at the membrane surface can be found in the Supplementary material). This dynamic is quite different from the one observed with an HWS-0.8 emulsion (Figure 5 J, K, L) consisting of droplets that are initially smaller (~10 μm) and coalesce into ~30 μm droplets over the ~1.5 h filtration test. It should be noted that the droplets that migrate to the membrane surface and attach only represent a subpopulation of the entire emulsion.

Magnified views of the stages of *droplet clustering* and *droplet deformation* are shown in Figure 5 J.1 and Figure 5 C.1 respectively. Image J.1 shows multiple oil droplets clustering around a few membrane pores, while image C.1 illustrates oil droplets in a cluster that are deformed to adapt polyhedral shapes.

The average oil rejection by the PCTE membrane was 97.2%±0.01% and 98.5%±0.01% in filtrations of HWS-0.1 and HWS-0.8 emulsions, respectively. Some oil droplets smaller than the pore size (5 μm) permeated the membrane during the DOTM tests. Most of the smaller droplets, however, attached to the membrane surface and formed clusters; over the longer term these droplets either coalesced into droplets too large to enter membrane pores or meandered toward a pore and eventually permeated through the membrane. Droplets larger than the pore diameter could permeate the membrane as well.

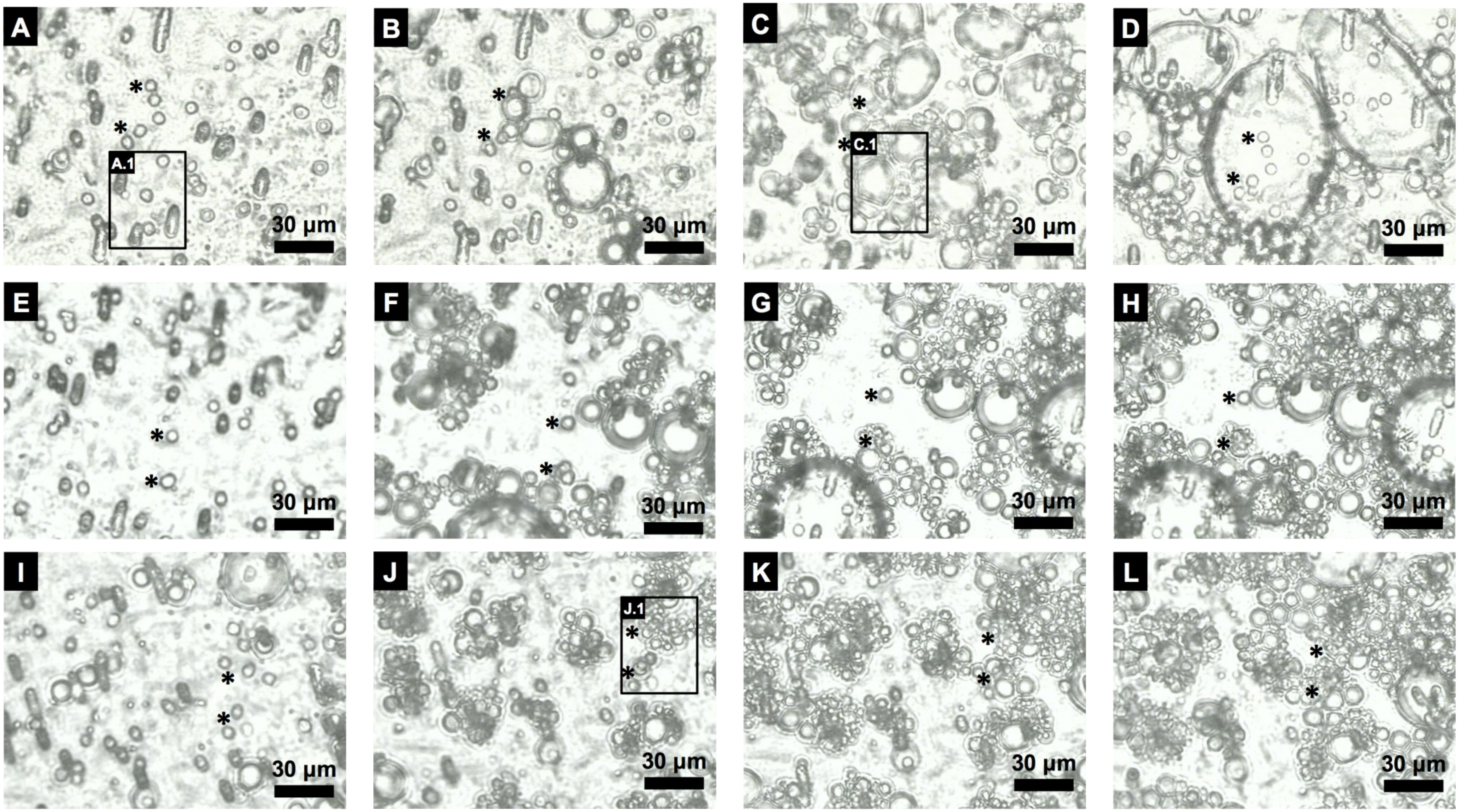

Figure 5: Transient behavior of oil droplets at the surface of polycarbonate track-etch membrane (d_{pore} = 5 μm) during crossflow microfiltration of hexadecane-water-SDS emulsions with different concentrations of surfactant: 0.1 mM (B, C, D), 0.4 mM (F, G, H) and 0.8 mM (J, K, L). Images A, E, I correspond to t = 0 when the membrane is unfouled. The direction of the crossflow (v_{cf}= 0.1 m/s) was from left to right in the images. The asterisks (*) denote a specific location on the membrane to aid in the comparison of images in each row (see Figure 8 for time stamps of images shown in columns 2 – 4).

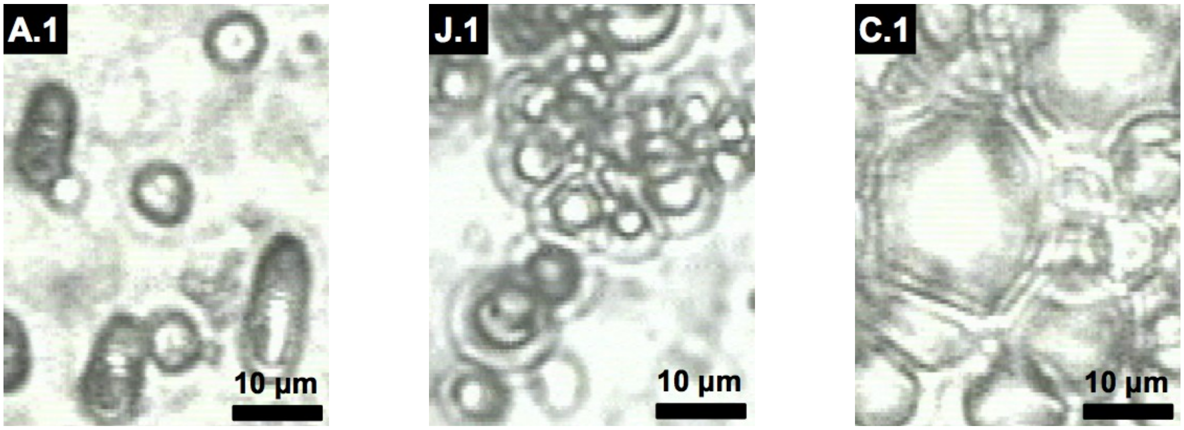

Figure 5 (continued): Magnified views of insets from Figure 5 A, J, and C: clean PCTE membrane (A.1); a PCTE membrane during *droplet attachment and clustering* stage (J.1) and a PCTE membrane during the *droplet deformation* stage (C.1).

As shown in Figure 6 a droplet ~15 µm in diameter passed through the PCTE membrane. (A video of the permeation event can be found in the Supplementary material). Notably, eq. (1) predicts that the pressure employed in the test (~0.01 bar) is ~8 times below ΔP_{crit} required for permeation. We attribute this discrepancy to two effects not accounted for in eq. (1): the presence of crossflow and the "cluster effect" when the crossflow drag on cluster-forming droplets accumulates and reaches maximum for the droplet pinned at the pore.

Another possibility for oil break-through is partial permeation resulting from a break-up of a droplet at the pore entry and permeation of only the part of the droplet that was in the pore during the "necking" process as the break-up occurred. In our earlier study [45], the break-up criterion was defined in terms of the critical capillary number, Ca_{crit}, which could be evaluated as:

$$Ca_{crit} \propto \frac{d_{pore}}{d_{drop}} \frac{1 + 1.048\lambda}{2 + 4.510\lambda} \tag{5}$$

where $\lambda = \mu_{oil}/\mu_w$. For a hexadecane-in-water emulsion, $\lambda \cong$ 3.44. Even for the membrane with the smaller d_{pore} (Anopore) and the largest droplet observed in DOTM tests (d_{drop} = 95 µm), Ca_{cf} was still smaller than the critical value ($Ca_{cf} \cong 0.74 Ca_{crit}$) indicating that partial permeation due to droplet breakup was not possible with either of the membranes.

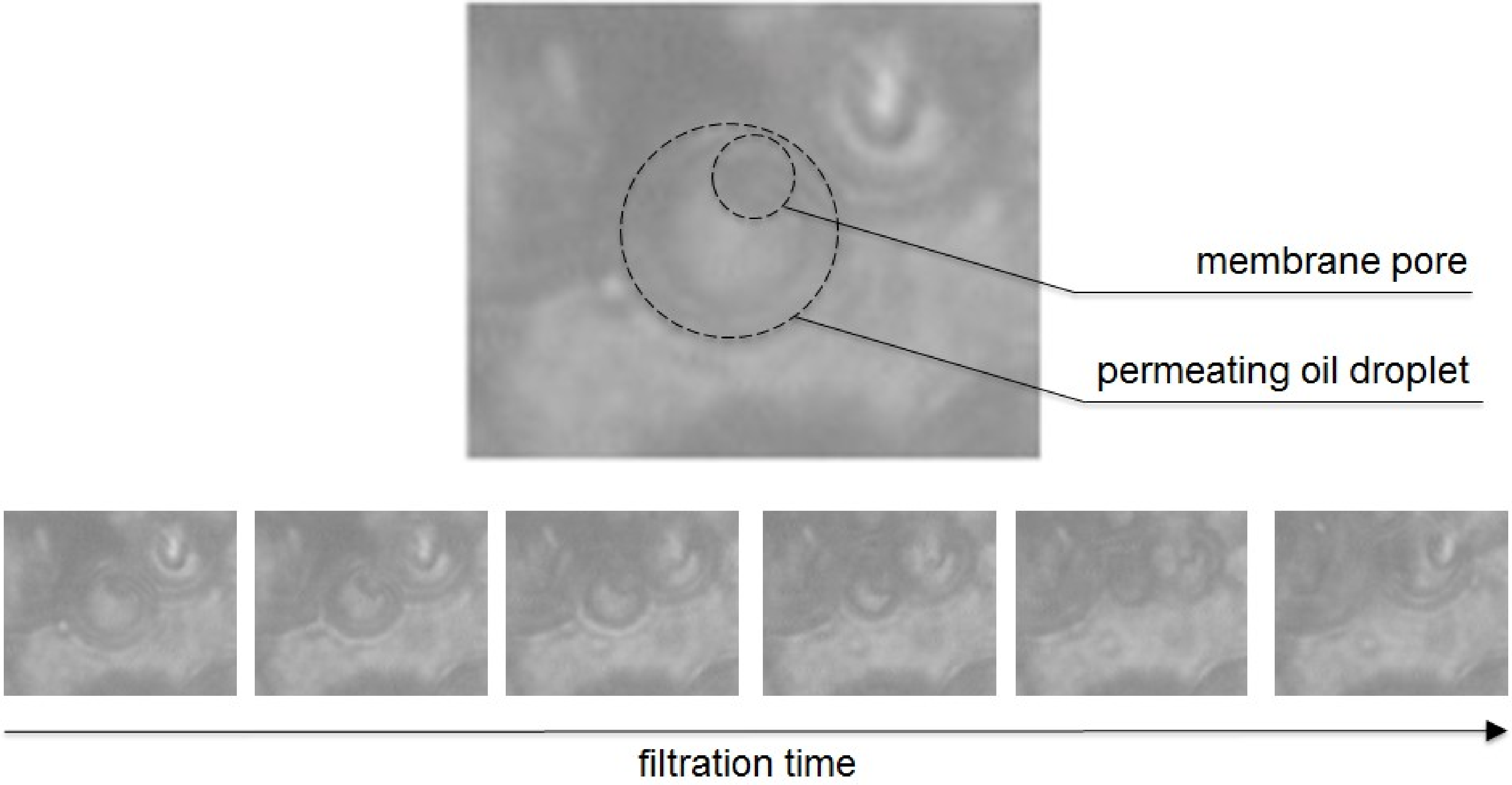

Figure 6: Different stages of oil droplet permeation through a 5 µm membrane pore in the case when $d_{drop} > d_{pore}$. The top image illustrates the initial condition of a droplet pinned at an entry to the membrane pore. The sequence of images below shows the evolution of the permeating droplet; the left most image in the sequence is the same as the large image with the pore and the droplet marked. This sequence took place in less than 2 seconds.

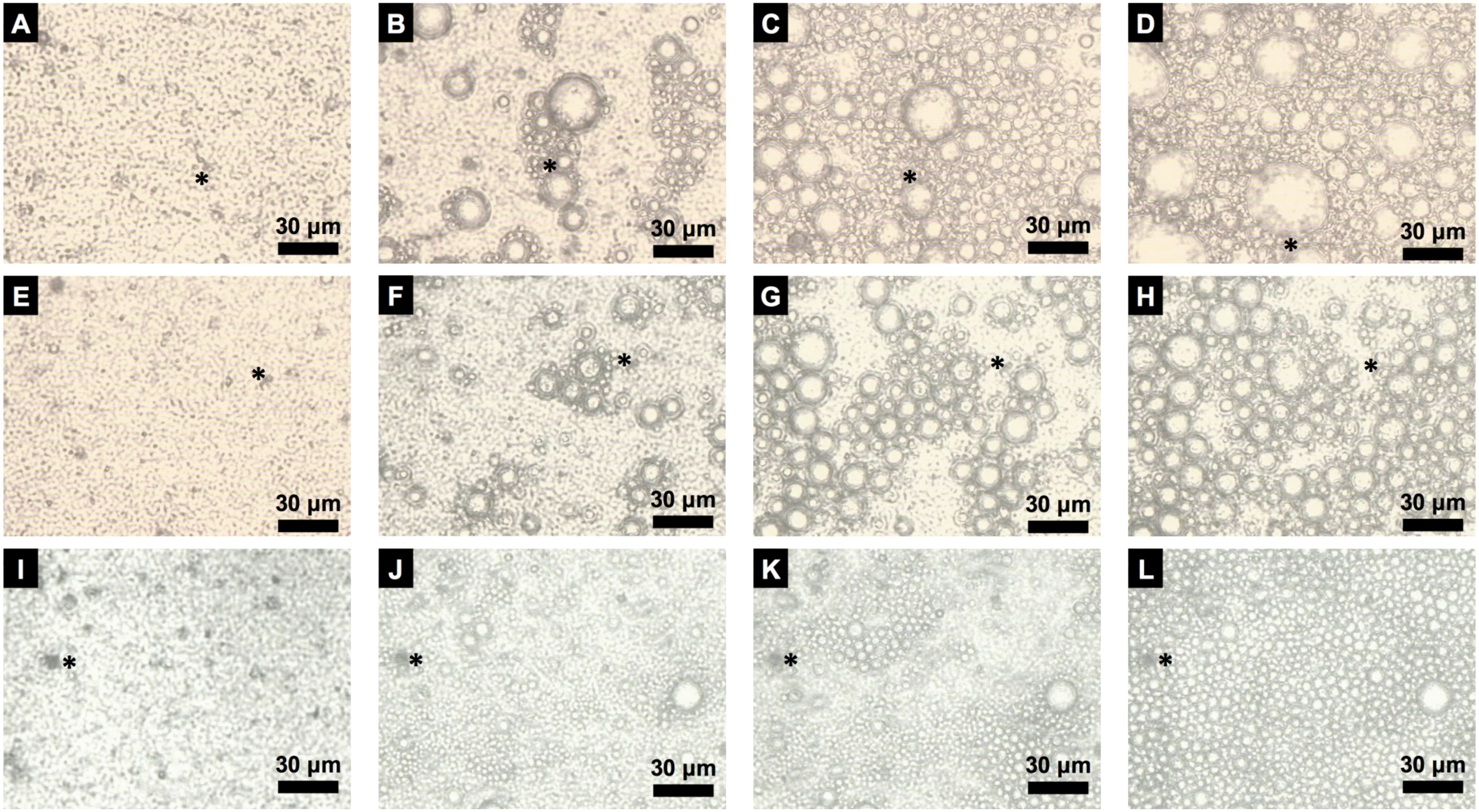

Figure 7: Transient behavior of oil droplets at the surface of Anopore membrane (d_{pore} = 0.2 µm) during crossflow microfiltration of hexadecane-water-SDS emulsions with different concentrations of surfactant: 0.1 mM (B, C, D), 0.4 mM (F, G, H) and 0.8 mM (J, K, L). Images A, E, I correspond to t = 0 when the membrane is unfouled. The direction of the crossflow (v_{cf} = 0.1 m/s) was from left to right in the images. The asterisks (*) denote a specific location on the membrane to aid in the comparison of images in the same row (see Figure 8 for time stamps of images shown in columns 2 – 4).

3.3.2. Microfiltration with Anopore membranes (d_{pore} = 0.2 μm)

Analogous to Figure 5, Figure 7 shows representative DOTM images from three separate filtration tests with Anopore membranes (d_{pore} = 0.2 μm) and different surfactant concentrations. Each of the three rows of images in Figure 5 corresponds to a filtration experiment with an emulsion with a different concentration of surfactant (0.1, 0.4, or 0.8 mM) and, accordingly, different interfacial tension (39.3, 35.0, or 30.9 mN/m). As in Figure 5, the first column (Figure 7 A, E, I) shows images of clean membranes. All other images (columns 2, 3 and 4) represent different fouling stages that occur at different times into an experiment depending on the concentration of the surfactant (see Figure 8 for time stamps).

The three characteristic fouling stages are observed with the Anopore membrane as well. It is evident that the oil droplets in the emulsion decrease in size as the surfactant concentration is increased and the droplets are less likely to coalesce at the membrane surface. A comparison of images D, H and L clearly shows the impact that surfactant concentration has on the likelihood that the oil droplets will coalesce at the membrane surface. The oil droplets in image L are tightly packed together, but the lower interfacial tension provided by the 0.8 mM of SDS caused some resistance to coalescence; whereas image D shows easily coalescing deformed droplets due to the 0.1 mM of SDS and corresponding higher interfacial tension. Droplets accumulating on the surface of the Anopore membranes (Figure 7) were smaller and more narrowly distributed in size.

A comparison of the images in Figure 5 and Figure 7 demonstrate that there are two key differences in the observed droplet behavior in filtration tests with the two types of membranes. First, the droplets tended to cover the entire Anopore membrane before the clusters of droplets got compressed and possibly coalesced; whereas the oil droplets attached to the PCTE membrane tended to compress and coalesce when large portions of the membrane were still unfouled. Both Figure 5 and Figure 7 demonstrate that as surfactant concentration increases, the likelihood that the compressed droplets will coalesce decreases.

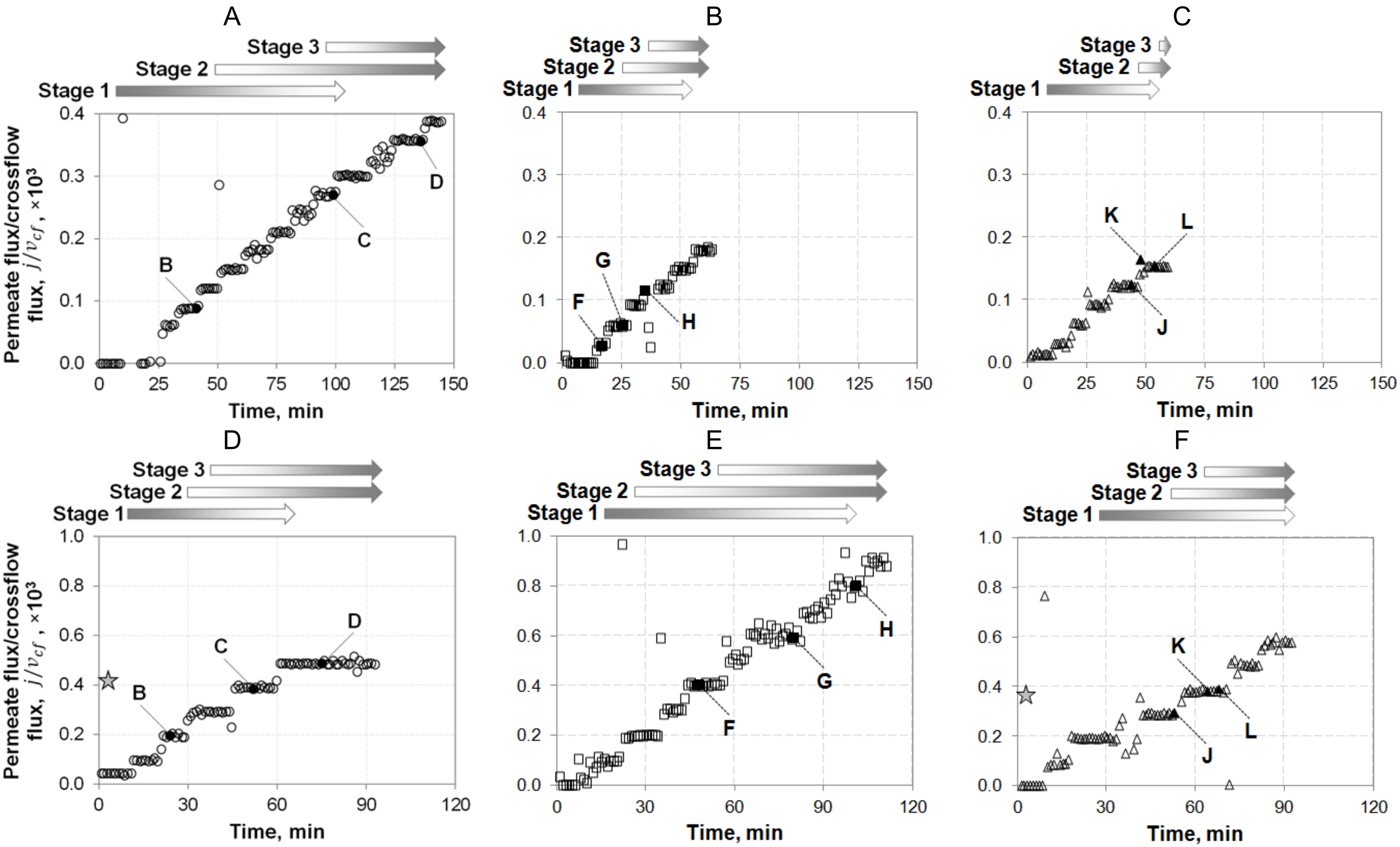

Figure 8: Attachment and clustering (stage 1), deformation (stage 2), and coalescence (stage 3) of hexadecane droplets on the surface of 0.2 µm pore size Anopore membrane (A, B, C) and 5 µm pore size PCTE (D, E, F) in experiments with increasing permeate-to-crossflow ratio and different surfactant concentrations: 0.1 mM SDS, σ= 39.3 mN/m (A, D); 0.4 mM SDS, σ = 35.0 mN/m (B, E); and 0.8 mM SDS, σ= 30.8 mN/m (C, F). Capital letters mark times when corresponding images shown in Figure 5 and Figure 7 were recorded. The crossflow velocity is all tests was 0.1 m/s.

Second, DOTM filtration tests clearly showed small oil droplets passing though the 5 μm PCTE pores as well as slightly larger droplets deforming and squeezing through the pores. No evidence was captured to show that oil droplets were able to penetrate the 0.2 μm Anopore membrane pores, but the 320X magnification of the microscope used during these filtration tests was not sufficient to differentiate between the individual 0.2 μm membrane pores meaning that permeation cannot be definitively ruled out.

3.4 The sequence of membrane fouling stages as a function of membrane type and emulsion stability.

The DOTM tests were conducted to screen for a range of fouling conditions; the sequence and duration of the three fouling stages (see section 3.3) are demonstrated in Figure 8. While the three stages occur sequentially for individual oil droplets and their clusters, the stages could overlap significantly when an ensemble of droplets on the entire membrane surface is considered. With the continual step-wise increase in permeate flux in the DOTM tests, the changing behavior of oil droplets could be interpreted as either one stage or a superposition of two or three fouling stages.

The determination for the beginning of each stage was subjective and based on images and videos captured throughout each of the filtration tests. Figure 8 represents six individual experiments; three of which were conducted with PCTE membranes (d_{pore} = 5 μm) while the other three tests used Anopore membranes (d_{pore} = 0.2 μm). Both types of membranes were tested using emulsions of varying SDS concentrations (0.1 mM, 0.4 mM and 0.8 mM).

For the emulsions containing 0.1, 0.4, and 0.8 mM of SDS, PCTE filtration tests show a coalescence stage beginning at a permeate flux to crossflow flux ratios of $0.3 \cdot 10^{-3}$, $0.4 \cdot 10^{-3}$, and $0.4 \cdot 10^{-3}$, respectively. Thus, as expected, the coalescence began at a lower permeate flux to crossflow flux ratio for the least stabilized HWS-0.1 emulsion (i.e., more stable emulsions required additional drag available at higher permeate flows to coalesce). In contrast, in the tests with the Anopore membranes, a higher permeate flux was needed to initiate the coalescence stage for the HWS-0.1 emulsion (j/v_{cf} = $0.27 \cdot 10^{-3}$) than for more stable HWS-0.4 and HWS-0.8 emulsions (j/v_{cf} = $0.12 \cdot 10^{-3}$ and $0.15 \cdot 10^{-3}$, respectively). One possible explanation for this trend is that higher stability facilitates droplet's movement along the surface leading to larger clusters and higher likelihood of coalescence. The above interpretations are based on a small sample size and, therefore, are tentative. One consistent trend that was observed for each of the three emulsion types was that the coalescence began at higher permeate fluxes for PCTE membranes pointing to the general conclusion that pore morphology (Table 1) affects oil coalescence at the membrane surface; the reasons for this trend are not yet clear.

3.5 Constant pressure crossflow filtration tests

A separate set of crossflow filtration experiments (Figure 2B) with PCTE membranes (d_{pore} = 5 μm) only were performed in the constant transmembrane pressure regime. (This was in contrast to the flux-controlled DOTM tests (sections 3.2 – 3.4) wherein by adjusting the pumping rate, the permeate flux was incrementally increased throughout each experiment leading to corresponding increases in the transmembrane pressure.) The retentate was returned to the feed tank positioned at a height that created just enough pressure to make the initial permeate flux match the permeate flux during the coalescence stage of the DOTM tests (~$4.2 \cdot 10^{-5}$ m/s); these experimental conditions are represented by stars in Figure 8 D and F. The three replicate filtration experiments with HWS-0.1 emulsions (Figure 9A) showed significantly more variability in the decline of permeate flux than what was observed in tests with the HWS-0.8 emulsions (Figure 9B). This difference is consistent with the higher stability of HWS-0.8. Momentary increases in the permeate flux during the last hour of the HWS-0.1 tests occurred when large oil droplets left the filtration cell into the retentate stream. The large oil droplets swept off the membrane opened up more membrane area for permeation and could have blocked the retentate line leading to a transient increase in the backpressure to give higher permeate flux. The flux data from the constant pressure filtration tests (Figure 9) corroborate the qualitative DOTM results (Figure 5) for the coalescence stage of fouling:

as the large oil droplets formed and grew with the HWS-0.1 emulsions, after ~1 h of continual coalescence at the membrane surface the

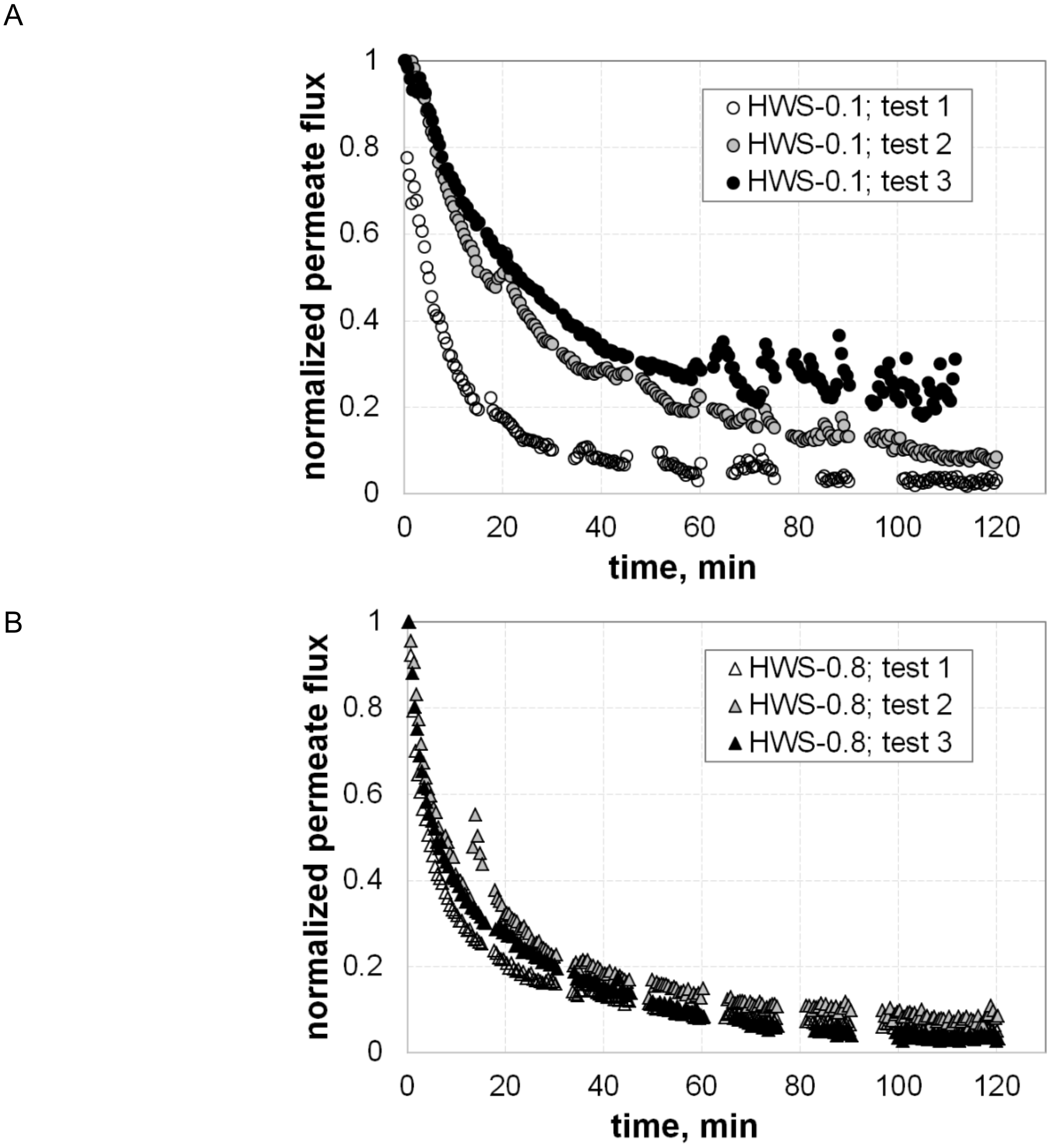

Figure 9: Permeate flux behavior in crossflow microfiltration tests with HWS-0.1 emulsions (A) and HWS-0.8 emulsions (B) and PCTE membranes (d_{drop} = 5 μm). The experiments were performed in a constant pressure regime ($\Delta P = 0.2$ bar) and with a constant crossflow velocity v_{cf} = 0.1 m/s (3.6 10^5 L/($m^2 \cdot h$)). The hydraulic resistance of clean membranes averaged over tests 1 – 3 with HWS-0.1 and tests 1 and 3 with HWS-0.8 was $(3.37 \pm 0.11) \cdot 10^{10}$ m^{-1}; the hydraulic resistance of the clean membrane in test 2 with HWS-0.8 was $4.98 \cdot 10^{10}$ m^{-1}.

droplets were sufficiently large for the crossflow drag to remove them from the membrane (see section 3.6). In contrast, during tests with more stable HWS-0.8 emulsions, oil droplets did not coalesce to the point that the crossflow drag could dislodge them from the membrane surface.

In analogy with the cleaning effect of the crossflow during the separation of colloids and larger solid particles, the crossflow appears to lead to pseudo steady state permeate flux during the separation of liquid-liquid emulsions. In the former case, the membrane deposit of solid particles grows into a thick multilayer structure ("membrane cake") that constricts the membrane channel to a point where the crossflow velocity becomes sufficiently high to scour the fouling particles at a rate equal to the rate of their addition to the cake due to permeate flow. In the latter case of the separation of liquid-liquid emulsions, the deposited droplets generally do not seem to form multilayer deposits (although occasional deposition of smaller droplets on top of the larger ones was observed in DOTM tests); instead, droplets coalesce until the size of the coalesced droplet is sufficiently large for the crossflow drag force to overcome the permeation drag and sweep the droplet off the membrane surface. Because the main mechanism of flux decline appears to be pore blockage by droplets, the % decline of the flux can be interpreted as the % of blocked pores. For example, the ~95% decline in the permeate flux observed in tests with HWS-0.8 emulsions (Figure 9B) indicates that only ~5% of the surface pores remain open while the rest of the pores are plugged by droplets pinned at pore entries. In other studies [7] the low values of flux after fouling by oil were attributed to the very high hydraulic resistance of the oil layer on the membrane surface. Our results show that low flux can be achieved even at sub-monolayer coverage and is due to pore plugging by oil droplets. This should be more pronounced for Anopore and track-etch membranes that both have straight-through pores than for membranes with pore interconnectivity typical for polymeric membranes prepared by phase inversion.

3.6 Force balance on an oil droplet pinned at an entry to a cylindrical pore

The force balance analysis employed in this work follows the approach we applied earlier to solid particles on the membrane surface [56]. The moment of hydrodynamic forces acting on a particle about its point of contact with a surface (pivot) can be used as a criterion of whether the particle remains pinned on the surface or is swept off [57]. Herein we apply such criterion to the case of an oil droplet resting at the entry to a cylindrical pore of a membrane (Figure 10; also see Supplementary material, Figure S3).

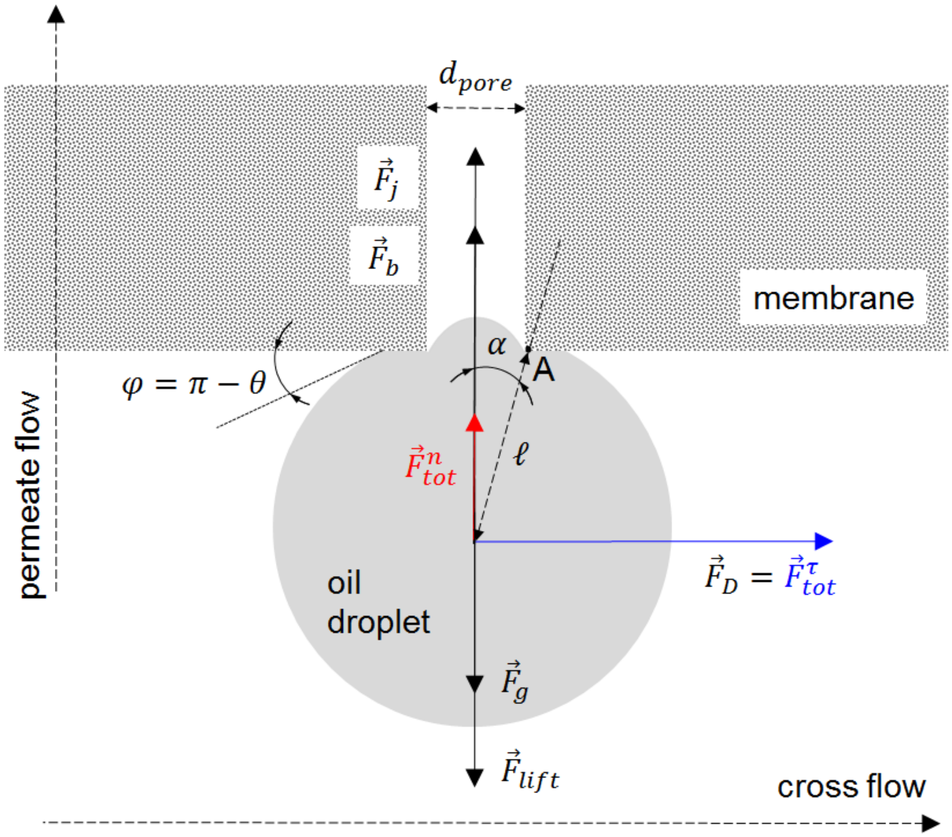

Figure 10: Hydrodynamic forces acting on an oil droplet positioned at the entry to a cylindrical pore of a membrane. The angles θ and α are the droplet's contact angle and angle of repose, respectively. See the text for the definitions of forces. Forces are not drawn to scale. In DOTM tests, the microscope was located above the semitransparent membrane (i.e. on the permeate side) and the focal plane of the microscope was on the feed side where oil droplets were accumulating.

The moment of the sum of forces acting tangentially to the membrane surface, F^{τ}_{tot}, around the pivot A is $F^{\tau}_{tot}\ell\cos(\alpha)$, where α is the angle of repose and ℓ is the lever arm of the moment (α and ℓ defined as shown in Figure 10; also see Supplementary material, section S3). The moment of the sum of forces acting normal to the membrane surface, F_{tot}^{n}, around the pivot A is $F_{tot}^{n}\ell\sin(\alpha)$ (presuming the net force points upward). The sum of moments (of forces) is given by:

$$M = \ell(F_{tot}^{\tau}\cos\alpha\ - F_{tot}^{n}\sin\alpha) \tag{6}$$

Eq. (6) written for the zero value of the net moment of all forces acting on the oil droplet:

$$F_{tot}^{\tau} = F_{tot}^{n}\tan\alpha \tag{7}$$

can be solved to determine the diameter of the largest droplet that remains pinned at the membrane pore.

F_{tot}^{τ} is equal to the drag force, which can be approximated using a modified Stokes equation [58]:

$$F_{tot}^{\tau} = F_D = C_1 3\pi\mu_w d_{drop}\left[v_{cf}\right]_{y=\frac{1}{2}d_{drop}} \tag{8}$$

where the crossflow velocity, v_{cf}, is evaluated as the fluid velocity at the center of the droplet (i.e. at a distance $\frac{1}{2}d_{drop}$ away from the membrane surface) and C_1 = 1.7009 is a coefficient that accounts for the presence of the membrane. It can be easily shown (see Supplementary material) that $\left[v_{cf}\right]_{y=\frac{1}{2}d_{drop}} = 3\bar{v}_{cf}\frac{d_{drop}}{H}$, where $\bar{v}_{cf}$ is the average crossflow velocity in the membrane channel. In all DOTM and constant pressure crossflow filtration tests, the crossflow rate was maintained at the same value so that $\bar{v}_{cf}$ = 0.1 m/s.

The force F_{tot}^{n} is the sum of all hydrodynamic forces that act on the droplet in the direction normal to the membrane surface:

$$F_{tot}^{n} = F_j - F_{lift} + F_b - F_g \tag{9}$$

The sum of buoyancy and gravitational forces is given by

$$F_b - F_g = (\rho_w - \rho_{oil})g\frac{\pi d_{drop}^3}{6} \tag{10}$$

The drag force exerted on the droplet in contact with the membrane surface by the flow permeating the membrane, F_j, is given by a modified version of the Stokes law:

$$F_j = \phi 3\mu_w\pi d_{drop}j \tag{11}$$

that includes the wall correction factor, ϕ, derived by Goren [59] for a particle in contact with a thin membrane:

$$\phi = \sqrt{\frac{R_m d_{drop}}{3} + 1.072^2} \tag{12}$$

where R_m is the hydraulic resistance of the membrane. The expression (12) is chosen because a thin membrane is a better representation of the straight-though pore membranes such as PCTE and Anopore than the boundary condition of an infinite porous half-space that Sherwood employed [60] in deriving an alternative expression for the wall correction factor.

The inertial lift force, F_{lift}, on a droplet attached to a wall is given by [61]

$$F_{lift} = 0.576\rho_w \dot{\gamma}^2 d_{drop}^4 \tag{13}$$

where $\dot{\gamma}$ is the shear rate of an unperturbed flow; we estimate $\dot{\gamma}$ by the value of the shear rate half a droplet diameter away from the membrane surface (eq. (3)). Note that eq. (12) and eq. (13) are for solid, non-deformable particles. Applied to oil droplets the expressions may provide estimates but not exact answers because of the finite viscosity of the oil and a partial entry of droplets into pores.

For membranes with d_{pore} = 5 µm, the condition given by eq. (7) is met for droplets with $d_{drop}^{crit} \approx$ 40 µm in 0.1 mM SDS solution (Figure 11) and $d_{drop}^{crit} \approx$ 36 µm in 0.8 mM SDS solution (not shown). For droplets of this critical size the tangential ($F_{tot}^{\tau}\ell \cos\alpha$) and normal ($F_{tot}^{n}\,\ell \sin\alpha$) components of the moment balance each other out because the lift force ($F_{lift} \propto d_{drop}^4$) counteracting the permeate drag grows to be sufficiently large. Thus, the force balance analysis predicts that droplets $\lesssim d_{drop}^{crit}$ would remain pinned while larger droplets would be swept off the surface by the crossflow drag. This prediction is in a qualitative agreement with visualization results. The deviations can be attributed to the approximate nature of the force balance calculations. Figure 9 presents an idealized scenario where a symmetric droplet interacts with an unperturbed flow. In reality, most droplets are positioned in the vicinity of other droplets, and as such the drag force exerted by the crossflow on the droplets should decrease due to the shielding effect. Further, the force balance relies on the assumption that the droplet is positioned on one pore. However, as was observed in DOTM tests (e. g., Figure 5 C, D, G, H, L) there may be multiple pores under one droplet. A calculation that is based on the PCTE membrane morphology data (Table 1) and droplet geometry shows droplets larger than 19 μm cover, on average, more than one pore.. For example, the droplet of d_{drop}^{crit} = 40 μm covers, on average, between 2 and 3 pores.

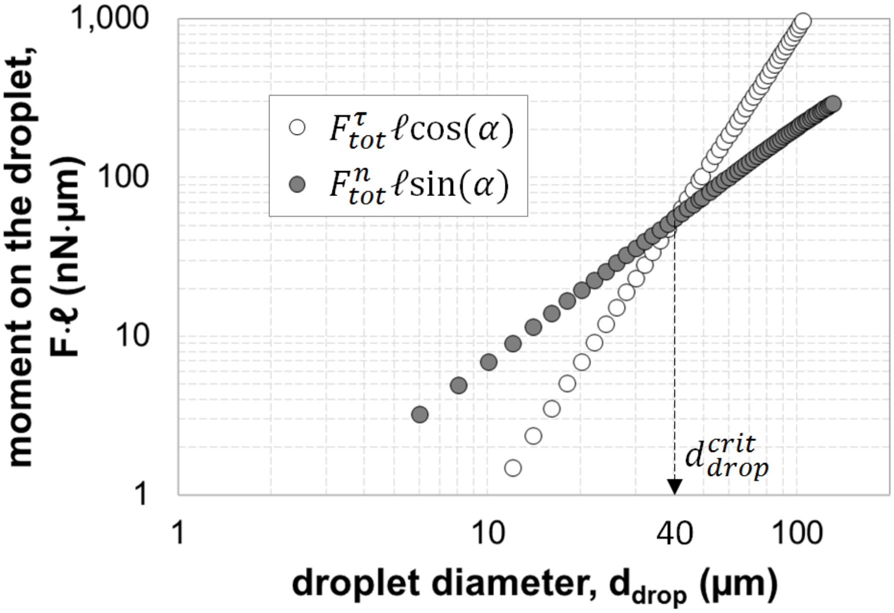

Figure 11: Moment balance on an oil droplet of diameter d_{drop} positioned at a cylindrical pore (d_{pore} = 5 μm) of a PCTE membrane.
Conditions: j = 8.78·10^{-5} m/s; $\bar{v}_{cf}$ = 0.1 m/s; θ = 135° (0.1 mM SDS solution), μ_w = 1.002·10^{-3} kg/(m·s), ρ_w = 998 kg/m^3; ρ_{oil} = 770 kg/m^3; R_m = 3.37·10^{10} m^{-1}. The expression for the lever arm of the moments, ℓ, is provided in the Supplementary material.

The results indicate that membrane fouling by emulsified oil is controlled by droplet coalescence and crossflow shear: the transport of oil to the membrane surface by the permeate flow is balanced by the shear-induced removal of the droplets that coalesce to exceed a critical size. Thus membrane surfaces that promote droplet coalescence may be more resistant to membrane fouling by oil when operated in a crossflow configuration as long as intrapore fouling is avoided and droplets are removed prior to the formation of a contiguous film. The fouling dynamic may be different for more stable oil droplets where compressible multilayer gel emulsions of low hydraulic permeability are likely to form and control permeate flux.

4. Conclusions

The study describes the first application of a direct visualization technique to capture real-time images of a membrane surface under conditions of fouling by emulsified oil in the presence of crossflow. DOTM experiments with hexadecane-water-SDS emulsions revealed three characteristic stages of membrane fouling by oil: 1) droplet attachment and clustering, 2) droplet deformation, and 3) droplet coalescence. Increasing concentration of SDS from 0.1 mM to 0.8 mM decreased the interfacial tension of the emulsion from 39.3 mN/m to 30.8 mN/m, shifted the size distribution of suspended droplets toward smaller sizes and stabilized the emulsion as manifested by a decreased propensity of droplets to coalesce on the membrane surface. Droplet permeation was observed for droplet's sized slightly above the membrane pore size and smaller. PCTE membranes (d_{pore} = 5 μm) rejected at least 96% of oil while Anopore membranes (d_{pore} = 0.2 μm) appeared to reject oil completely. The force balance on an oil droplet pinned on a single pore at the membrane surface predicted the critical size of a droplet that is not swept away by the crossflow; the predicted droplet diameter of 49 μm was in qualitative agreement with the DOTM observations in experiments with 5 μm pore size membranes. A separate set of crossflow filtration tests in a constant pressure regime with 5 μm pore size membranes demonstrated that permeate flux reaches a steady state value. The results indicate that membrane fouling by emulsified oil (in this study's range of interfacial tensions), is controlled by droplet coalescence and crossflow shear: the transport of oil to the membrane surface by the permeate flow is balanced by the shear-induced removal of the droplets that coalesce to exceed a critical size. This is in contrast to the scenario where viscoelastic multilayer deposit (i.e. gel emulsion) of low hydraulic permeability controls the permeate flux. Additional work with emulsions of varying degrees of stability would help elucidate the relative importance of these two fouling scenarios under different conditions..

Acknowledgements

This material is based upon work supported in part by the National Science Foundation Partnerships for International Research and Education program under Grant IIA-1243433 and the National Science Foundation Graduate Research Fellowship for Emily N. Tummons under Grant No. DGE-0802267. We also acknowledge funding from NTU iFood Research Grant (M4081465.120) and Singapore Ministry of Education Academic Research Fund Tier 2 (MOE2014-T2-2-074). The Singapore Membrane Technology Center (SMTC) acknowledges support from Singapore's Economic Development Board (EDB). We thank Drs. Wu Bing and Farhad Zamani (Nanyang Technological University) for their help with DOTM training at the Singapore Membrane Technology Center and Mr. Hang Shi (Michigan State University) for his assistance with contact angle measurements.

Nomenclature

α	angle of repose
$\dot{\gamma}$	shear rate
θ	contact angle
μ_{oil}	dynamic viscosity of the hexadecane (dispersed phase)
μ_{w}	dynamic viscosity of water (continuous phase)
ρ_{oil}	density of oil
ρ_{w}	density of water
σ	interfacial tension
ϕ	wall correction factor
Bo	Bond number
Ca_{cf}	capillary number associated with crossflow
Ca_{pf}	capillary number associated with permeate flow
Ca_{crit}	critical capillary number characteristic for oil break-up condition
C_f	initial concentration of oil in the feed emulsion
C_p	concentration of oil in the permeate
d_{drop}	oil droplet diameter
d_{drop}^{crit}	critical diameter of the droplet
d_{pore}	membrane pore diameter
F_b	buoyancy force
F_D	drag force
F_g	gravity force
F_j	drag force due to permeate flow
F_{lift}	lift force
F_{tot}^{n}	sum of forces acting on an oil droplet in the direction normal to the membrane surface
F_{tot}^{τ}	sum of forces acting on an oil droplet in the direction parallel to the

	membrane surface
g	acceleration due to gravity
H	height of the membrane channel
j	permeate flux
ℓ	lever arm of the moments on an oil droplet
M	sum of moments acting on an oil droplet
ΔP	transmembrane pressure
ΔP_{crit}	critical transmembrane pressure required for an oil droplet to enter a membrane pore
R	rejection of oil by the membrane
Re	Reynolds number
R_m	hydraulic resistance of the membrane
v_{cf}	crossflow velocity
$\bar{v}_{cf}$	average crossflow velocity in the membrane channel
W	width of the membrane channel

List of Tables

Table 1: Morphological characteristics of the polycarbonate track-etch (PCTE) and Anopore membranes employed in this study

[#] provided by the manufacturer.

[†] applies to all PCTE membranes used in this study regardless of the supplier

List of Figures

Figure 1: Number of publications with a) both “oil” and “ultrafiltration” in the title and b) both “oil” and “microfiltration” in the title. Source: Google Scholar. Retrieved: November 1, 2015

Figure 2: Schematic illustration of the Direct Observation Through the Membrane apparatus (A) and the crossflow microfiltration system (B).

Figure 3: Volume-based (A) and number-based (B) droplet size distributions for the three SDS-stabilized hexadecane-water emulsions used in the DOTM and constant pressure microfiltration tests.

Figure 4: Critical pressure for an oil droplet to enter a membrane pore as a function of oil droplet size, membrane pore size, and interfacial tension of the oil-water emulsion. The calculation is based on eq. (1) and is for Anopore (d_{pore} = 0.2 μm) and polycarbonate PCTE (d_{pore} = 5 μm) membranes. The operational domain represents the range of oil droplet sizes in the HWS-0.1 and HWS-0.8 emulsions and the range of transmembrane pressures employed in the DOTM and constant pressure microfiltration tests

Figure 5: Transient behavior of oil droplets at the surface of polycarbonate track-etch membrane (d_{pore} = 5 μm) during crossflow microfiltration of hexadecane-water-SDS emulsions with different concentrations of surfactant: 0.1 mM (B, C, D), 0.4 mM (F, G, H) and 0.8 mM (J, K, L). Images A, E, I correspond to t = 0 when the membrane is unfouled. The direction of the crossflow (v_{cf}= 0.1 m/s) was from left to right in the images. The asterisks (*) denote a specific location on the membrane to aid in the comparison of images in each row (see Figure 8 for time stamps of images shown in columns 2 – 4). Magnified views of insets from Figure 5 A, J, and C: clean PCTE membrane (A.1); a PCTE membrane during *droplet attachment and clustering* stage (J.1) and a PCTE membrane during the *droplet deformation* stage (C.1).

Figure 6: Different stages of oil droplet permeation through a 5 μm membrane pore in the case when $d_{drop} > d_{pore}$. The top image illustrates the initial condition of a droplet pinned at an entry to the membrane pore. The sequence of images below shows the evolution of the permeating droplet; the left most image in the sequence is the same as the large image with the pore and the droplet marked. This sequence took place in less than 2 seconds.

Figure 7: Transient behavior of oil droplets at the surface of Anopore membrane

(d_{pore} = 0.2 µm) during crossflow microfiltration of hexadecane-water-SDS emulsions with different concentrations of surfactant: 0.1 mM (B, C, D), 0.4 mM (F, G, H) and 0.8 mM (J, K, L). Images A, E, I correspond to t = 0 when the membrane is unfouled. The direction of the crossflow (v_{cf} = 0.1 m/s) was from left to right in the images. The asterisks (*) denote a specific location on the membrane to aid in the comparison of images in the same row (see Figure 8 for time stamps of images shown in columns 2 – 4).

Figure 8: Attachment and clustering (stage 1), deformation (stage 2), and coalescence (stage 3) of hexadecane droplets on the surface of 0.2 µm pore size Anopore membrane (A, B, C) and 5 µm pore size PCTE (D, E, F) in experiments with increasing permeate-to-crossflow ratio and different surfactant concentrations: 0.1 mM SDS, σ= 39.3 mN/m (A, D); 0.4 mM SDS, σ = 35.0 mN/m (B, E); and 0.8 mM SDS, σ= 30.8 mN/m (C, F). Capital letters mark times when corresponding images shown in Figure 5 and Figure 7 were recorded. The crossflow velocity is all tests was 0.1 m/s.

Figure 9: Permeate flux behavior in crossflow microfiltration tests with HWS-0.1 emulsions (A) and HWS-0.8 emulsions (B) and PCTE membranes (d_{drop} = 5 µm). The experiments were performed in a constant pressure regime ($\Delta P =$ 0.2 bar) and with a constant crossflow velocity v_{cf} = 0.1 m/s (3.6 10^5 L/(m^2·h)). The hydraulic resistance of clean membranes averaged over tests 1 – 3 with HWS-0.1 and tests 1 and 3 with HWS-0.8 was (3.37 ± 0.11)·10^{10} m^{-1}; the hydraulic resistance of the clean membrane in test 2 with HWS-0.8 was 4.98·10^{10} m^{-1}.

Figure 10: Hydrodynamic forces acting on an oil droplet positioned at the entry to a cylindrical pore of a membrane. The angles θ and α are the droplet's contact angle and angle of repose, respectively. See the text for the definitions of forces. Forces are not drawn to scale. In DOTM tests, the microscope was located above the semitransparent membrane (i.e. on the permeate side) and the focal plane of the microscope was on the feed side where oil droplets were accumulating.

Figure 11: Moment balance on an oil droplet of diameter d_{drop} positioned at a cylindrical pore (d_{pore} = 5 µm) of a PCTE membrane.
Conditions: j = 8.78·10^{-5} m/s; $\bar{v}_{cf}$ = 0.1 m/s; θ = 135° (0.1 mM SDS solution), μ_w = 1.002·10^{-3} kg/(m·s), ρ_w = 998 kg/m^3; ρ_{oil} = 770 kg/m^3; R_m = 3.37·10^{10} m^{-1}. The expression for the lever arm of the moments, ℓ, is provided in the Supplementary material.

References

[1] W.L. Adamson, M.W. Titus, Separation of oil in bilge water by semipermeable membrane, in, Naval Ship Research and Development Lab, Annapolis, MD, 1971.

[2] R.L. Goldsmith, S. Hossain, Ultrafiltration Concept for Separating Oil from Water, U. S. Coast Guard Rept. No. 4305.2/2, in, 1973.

[3] R.L. Goldsmith, D.A. Roberts, D.L. Burre, Ultrafiltration of soluble oil wastes, J. Water Poll. Control Fed., 46 (1974) 2183-2192.

[4] M. Cheryan, N. Rajagopalan, Membrane processing of oily streams. Wastewater treatment and waste reduction, J. Membr. Sci., 151 (1998) 13-28.

[5] J.K. Milić, A. Murić, I. Petrinić, M. Simonič, Recent developments in membrane treatment of spent cutting-oils: A review, Ind. Eng. Chem. Res., 52 (2013) 7603−7616.

[6] L.M. Hailemariam, A. Johnson, A. Roy, K. Olanrewaju, K. Reyntjens, Membranes for produced water treatment, in: E.M.V. Hoek, V.V. Tarabara (Eds.) Encyclopedia of Membrane Science and Technology, John Wiley & Sons, Inc., 2013.

[7] S. Yao, M. Costello, A.G. Fane, J.M. Pope, Non-invasive observation of flow profiles and polarisation layers in hollow fibre membrane filtration modules using NMR micro-imaging, J. Membr. Sci., 99 (1995) 207-216.

[8] F.F. Nazzal, M.R. Wiesner, Microfiltration of oil-in-water emulsions, Water Environ. Res., 68 (1996) 1187-1191.

[9] J.M. Pope, S. Yao, A.G. Fane, Quantitative measurements of the concentration polarisation layer thickness in membrane filtration of oil-water emulsions using NMR micro-imaging, J. Membr. Sci., 118 (1996) 247-257.

[10] R.G. Holdich, I.W. Cumming, I.D. Smith, Crossflow microfiltration of oil in water dispersions using surface filtration with imposed fluid rotation, J. Membr. Sci., 143 (1998) 263-274.

[11] I.W. Cumming, R.G. Holdich, I.D. Smith, The rejection of oil by microfiltration of a stabilised kerosene/water emulsion, J. Membr. Sci., 169 (2000) 147-155.

[12] A. Ullah, R.G. Holdich, M. Naeem, V.M. Starov, Stability and deformation of oil droplets during microfiltration on a slotted pore membrane, 401-402 (2012) 118– 124.

[13] F. Quemeneur, J.P. Schlumpf, Traitement des huiles solubles par ultrafiltration, Entropie, 93 (1980) 22-29.

[14] S. Lee, Y. Aurelle, H. Roques, Concentration polarization, membrane fouling, and cleaning in ultrafiltraton of soluble oil, J. Membr. Sci., 19 (1984) 23-38.

[15] P. Lipp, C.H. Lee, A.G. Fane, C.J.D. Fell, A fundamental study of the ultrafiltration of oil-water emulsions, J. Membr. Sci., 36 (1988) 161-177.

[16] N. Nabi, P. Aimar, M. Meireles, Ultrafiltration of an olive oil emulsion stabilized by an anionic surfactant, J. Membr. Sci., 166 (2000) 177-188.

[17] B. Chakrabarty, A.K. Ghoshal, M.K. Purkait, Ultrafiltration of stable oil-in-water emulsion by polysulfone membrane, J. Membr. Sci., 325 (2008) 427-437.

[18] H. Falahati, A.Y. Tremblay, Flux dependent oil permeation in the ultrafiltration of highly concentrated and unstable oil-in-water emulsions, J. Membr. Sci., 371 (2011) 239-247.

[19] D. Lu, T. Zhang, J. Ma, Ceramic membrane fouling during ultrafiltration of oil/water emulsions: Roles played by stabilization surfactants of oil droplets, Environ. Sci. Technol. , 49 (2015) 4235−4244.

[20] T. Kawakatsu, Y. Kikuchi, M. Nakajima, Visualization of microfiltration phenomena using microscope video system and silicon microchannels, J. Chem. Eng. Japan, 29 (1996) 399-401.

[21] Y. Matsumoto, T. Kawakatsu, M. Nakajima, Y. Kikuchi, Visualization of filtration phenomena of a suspended solution including O/W emulsion or solid article and membrane separation poperties of the solution, Water Res., 33 (1999) 929-936.

[22] A.B. Koltuniewicz, R.W. Field, T.C. Arnot, Cross-flow and dead-end microfiltration of oily water emulsion: 1. Experimental study and analysis of flux decline, J. Membr. Sci., 102 (1995) 193-207.

[23] E. Iritani, Y. Mukai, N. Katagiri, Y. I., Formation of gel emulsions by filtration-consolidation of o/w emulsions, J. Chem. Eng. Japan, 36 (2003) 590-596.

[24] L.-H. Ding, O. Akoum, A. Abraham, M.Y. Jaffrin, High shear skim milk ultrafiltration using rotating disk filtration systems, AIChE J., 49 (2003) 2433-2441.

[25] B.E. Reed, W. Lin, R. Viadero Jr., J. Young, Treatment of oily wates using high shear rotary ultrafiltration, J. Environ. Eng. ASCE, 123 (1997) 1234-1242.

[26] A. Zaidi, K. Simms, S. Kok, The use of micro/ultrafiltration for the removal of oil and suspended solids from oilfield brines. , Water Sci. Technol., 25 (1992).

[27] S.M. Santos, M.R. Wiesner, Ultrafiltration of water generated in oil and gas production, Water Environ. Res., 69 (1997) 1120-1127.

[28] B. Dal Ferro, M. Smith, Global onshore and offshore water production, Exploration & Production: The Oil and Gas Review, in: Offshore Technology Conference (OTC) Edition, Houston, TX, 2007.

[29] TORR Canada's presentation, in: 14th International Petroleum Environmental Conference, Houston Texas, 2007.

[30] T. Frankiewicz, Understanding the fundamentals of water treatment. The dirty dozen - 12 common causes of poor water quality, in: 11th Produced Water Seminar, Houton, TX, 2001.

[31] S. Judd, H. Qiblawey, M. Al-Marri, C. Clarkin, S. Watson, A. Ahmed, S. Bach, The size and performance of offshore produced water oil-removal technologies for reinjection, Separ. Purif. Technol., 134 (2014) 241-246.

[32] The Paris Convention 1974 and The Oslo Convention 1972 (OSPAR), in, International Maritime Organization, 1974.

[33] E. Iritani, S. Matsumoto, N. Katagiri, Formation and consolidation of filter cake in microfiltration of emulsion-slurry, J. Membr. Sci., 318 (2008) 56-64.

[34] D.-Q. Cao, E. Iritani, N. Katagiri, Properties of filter cake formed during dead-end microfiltration of o/w emulsion, J. Chem. Eng. Japan, 46 (2013) 593-600.

[35] B.F. Ruth, G.H. Montillon, R.H. Montanna, Studies in filtration - I. Critical analysis of filtration theory, Ind. Eng. Chem. , 25 (1933) 76-82.

[36] B.F. Ruth, G.H. Montillon, R.H. Montanna, Studies in filtration - II. Fundamental axiom of constant-pressure filtration, Ind. Eng. Chem., 25 (1933) 153-161.

[37] H. Ohya, J.J. Kim, A. Chinen, M. Aihara, S.I. Semenova, Y. Negishi, O. Mori, M. Yasuda, Effects of pore size on separation mechanisms of microfiltration of oily water, using porous glass tubular membrane, Journal of Membrane Science, 145 (1998) 1-14.

[38] B. Hu, K. Scott, Microfiltration of water in oil emulsions and evaluation of fouling mechanism, Chemical Engineering Journal, 136 (2008) 210-220.

[39] B.K. Nandi, R. Uppaluri, M.K. Purkait, Treatment of oily waste water using low-cost ceramic membrane: Flux decline mechanism and economic feasibility, Separ. Sci. Technol., 44 (2009) 2840-2869.

[40] J. Mueller, Y. Cen, R.H. Davis, Crossflow microfiltration of oily water, J. Membr. Sci., 129 (1997) 221-235.

[41] B. Chakrabarty, A.K. Ghoshal, M.K. Purkait, Cross-flow ultrafiltration of stable oil-in-water emulsion using polysulfone membranes, Chem. Eng. J., 165 (2010) 447-456.

[42] V. Singh, M.K. Purkait, C. Das, Cross-flow microfiltration of industrial oily wastewater: Experimental and theoretical consideration, Separ. Sci. Technol., 46 (2011) 1213-1223.

[43] S. Yao, A.G. Fane, J.M. Pope, An investigatiop of teh fluidity of concentraton polarization layers in crossflow membrane filtration of an oil-water emulsion using chemical shift selective flow imaging, Magn. Reson. Imaging, 15 (1997) 235-242.

[44] T. Darvishzadeh, N.V. Priezjev, Effects of crossflow velocity and transmembrane pressure on microfiltration of oil-in-water emulsions, J. Membr. Sci., 423-424 (2012) 468-476.

[45] T. Darvishzadeh, V.V. Tarabara, N.V. Priezjev, Oil droplet behavior at a pore entrance in the presence of crossflow: Implications for microfiltration of oil-water dispersions, J. Membr. Sci., 447 (2013) 442-451.

[46] S. Peng, R.A. Williams, Controlled production of emulsions using a crossflow membrane, Part. Part. Syst. Charact., 15 (1998) 21-25.

[47] E. van der Zwan, K. Schroen, K. van Dijke, R. Boom, Visualization of droplet break-up in pre-mix membrane emulsification using microfluidic devices, Colloids Surface A, 277 (2006) 223-229.

[48] H. Li, A.G. Fane, H.G.L. Coster, S. Vigneswaran, Direct observation of particle deposition on the membrane surface during crossflow microfiltration, J. Membr. Sci., 149 (1998) 83-97.

[49] Y.P. Zhang, A.G. Fane, A.W.K. Law, Critical flux and particle deposition of bidisperse suspensions during crossflow microfiltration, J. Membr. Sci., 282 (2006) 189-197.

[50] c. rame-hart instruments, DROPimage Advanced v2.6 User Guide, in, 2012.

[51] A. Tuteja, W.M. Choi, G. H., R.E. Cohen, M.F. Rubner, Design parameters for superhydrophobicity and superoleophobicity, MRS Bull., 33 (2008) 752-758.

[52] T.F. Tadros, Emulsion Science and Technology: A General Introduction, in: T.F. Tadros (Ed.) Emulsion Science and Technology, Wiley-VCH Verlag GmbH & Co. KGaA, Weinheim, Germany,, 2009.

[53] P. Harmant, P. Aimar, Coagulation of colloids retained by porous wall, AIChE J., 42 (1996) 3523-3532.

[54] K.-J. Hwang, H.-C. Liu, W.-M. Lu, Local properties of cake in cross-flow microfiltration of submicron particles, J. Membr. Sci., 138 (1998) 181-192.

[55] G. Brans, R.G.M. van der Smana, C.G.P.H. Schroen, A. van der Padt, R.M. Boom, Optimization of the membrane and pore design for micro-machined membranes, J. Membr. Sci., 278 (2006) 239-250.

[56] P. Ji, A. Motin, W. Shan, A. Bénard, M.L. Bruening, V.V. Tarabara, Dynamic crossflow filtration with a rotating tubular membrane: Using centripetal force to decrease fouling by buoyant particles, Chem. Eng. Res. Des. (Submitted on June 8, 2015).

[57] W.-M. Lu, S.-C. Ju, Selective particle deposition in crossflow filtration, Separ. Sci. Technol., 24 (1989) 517-540.

[58] M.E. O'Neill, A sphere in contact with a plane wall in a slow linear shear flow, Chem. Eng. Sci., 23 (1968).

[59] S.L. Goren, The hydrodynamic force resisting the approach of a sphere to a plane permeable wall, J. Colloid Interface Sci., 69 (1979).

[60] J.D. Sherwood, The force on a sphere pulled away from a permeable half-space, PCH Phys Chem Hydrodyn, 10 (1988) 3-12.

[61] D. Leighton, A. Acrivos, The lift on a small sphere touching a plane in the presence of a simple shear flow, J. Appl. Math. Physics, 36 (1985) 174-178.